



Determination of complex refractive indices and optical properties of volcanic ashes in the thermal infrared based on generic petrological compositions

D. Piontek^{a,*}, A.J. Hornby^{b,c}, C. Voigt^{a,d}, L. Bugliaro^a, J. Gasteiger^e

^a Deutsches Zentrum für Luft- und Raumfahrt, Institut für Physik der Atmosphäre, Oberpfaffenhofen, Germany

^b Ludwig-Maximilians-Universität München, Department of Earth and Environmental Sciences, Munich, Germany

^c Cornell University, Department of Earth and Atmospheric Sciences, Ithaca, NY, USA

^d Johannes Gutenberg-Universität Mainz, Institut für Physik der Atmosphäre, Mainz, Germany

^e Universität Wien, Aerosol Physics and Environmental Physics, Vienna, Austria

ARTICLE INFO

Article history:

Received 8 September 2020

Received in revised form 4 January 2021

Accepted 6 January 2021

Available online 9 January 2021

Keywords:

Volcanic ash

Refractive index

Optical properties

Remote sensing

Thermal infrared

ABSTRACT

The spaceborne detection of volcanic ash clouds at infrared wavelengths helps to avoid regions with enhanced volcanic ash concentrations that pose a threat to aviation. Current volcanic ash data retrievals require detailed information on microphysical properties and the refractive index of volcanic ash, which are highly variable. Uncertainties in the latter currently limit the quality of volcanic ash nowcasts. Here, we introduce a novel method to calculate the complex refractive indices of volcanic ashes at wavelengths from 5 to 15 μm from measurements of their individual components based on generic petrological ash compositions. Thereby the refractive indices for volcanic glasses and bulk volcanic ashes of different chemical compositions are derived. The variability of the latter is mainly influenced by the silica content and the porosity and to a minor degree by the glass-to-crystals ratio. Calculating optical properties exhibits an equally large impact of bulk composition and grain size distribution, whereas particle shape is considered less important for particle sizes of the order 1 μm . Using these optical properties to determine brightness temperature differences between the 11 μm and 12 μm channels we show that the effect of ash composition is non-negligible for modern satellite instruments. Particularly, the dependence of the volcanic ash on the silica content (and to a much smaller extent on the glass-to-crystals ratio) is observable in its refractive index, its optical properties and the brightness temperature difference, indicating that composition might be retrievable to some degree by remote sensing methods.

© 2021 The Authors. Published by Elsevier B.V. This is an open access article under the CC BY license (<http://creativecommons.org/licenses/by/4.0/>).

1. Introduction

Volcanic ash emitted during eruptive activity poses a serious threat to critical infrastructure on the ground (Wilson et al., 2012) and to aircraft in operation, where contact with a volcanic ash plume or cloud can lead to damage and engine failure (Casadevall, 1994); here the term *plume* is used for volcanic emissions that are still attached to the vent, and *cloud* once they are detached. Incidents at distances of 1000 km and more have been reported (Guffanti et al., 2010). Therefore, the eruption of Eyjafjallajökull in 2010 led to the prolonged closure of large parts of the European air space (Schumann et al., 2011) with estimated economic losses in the aviation industry of \$1.7 billion (Budd et al., 2011).

In order to reduce the impact of future eruptions, satellite remote sensing methods have been developed and applied to monitor volcanic

ash plumes and clouds, and thereby calibrate/validate volcanic ash transport and dispersion models (Stohl et al., 2011; Dacre et al., 2016). For that polar orbiting as well as geostationary passive optical imagers are used (e.g. Pavolonis et al., 2015), often equipped with channels in the atmospheric window at 11 to 12 μm (Schmetz et al., 2002a; Watkin, 2003; Watson et al., 2004; Schmit et al., 2005; Bessho et al., 2016). Volcanic ash has been commonly detected using the difference in satellite-measured brightness temperatures at 11 μm and 12 μm (BTD_{11-12}), which is negative for volcanic ash clouds under certain conditions (e.g. small ash particles, low amounts of water or ice present, see Prata, 1989; Guéhenneux et al., 2015), but positive for ice clouds (Inoue, 1985) – the latter is another typical application of those channels. More recent volcanic ash retrieval algorithms (e.g. for mass concentrations or cloud top heights) make use also of other channels in the thermal infrared and visible spectrum (Prata and Grant, 2001; Pavolonis et al., 2006; Francis et al., 2012), hyperspectral data (Gangale et al., 2010; Clarisse et al., 2010) or more advanced concepts (Pavolonis et al., 2013; Pugnaghi et al., 2013; Piscini et al., 2014). Many of those are based on

* Corresponding author.

E-mail address: dennis.piontek@dlr.de (D. Piontek).

radiative transfer calculations, which in turn require the microphysical properties and the complex refractive index of the volcanic ash, Eq. (1), for the accurate simulation of brightness temperatures as a function of optical, micro- and macrophysical properties (e.g. Prata and Grant, 2001; Yu et al., 2002; Gangale et al., 2010; Pugnaghi et al., 2013; Ishimoto et al., 2016).

$$m = n + ik \quad (1)$$

Unfortunately, the volcanic ash properties are quite variable (Langmann, 2013), depending e.g. on the geographic location (Rogers, 2015) and the eruption style of the volcano (Polacci et al., 2019). Atmospheric processes further change the properties of the volcanic ash plumes and clouds (Langmann, 2013). In this study we focus on fine, distal ash, i.e. particles of a few micrometers in size which can travel within volcanic ash clouds thousands of kilometers. The corresponding typical properties are reviewed in the methods section of this paper.

The microphysical properties of volcanic ashes, in particular the particle size distribution and the particle shape, can have a large impact on their optical properties. Wen and Rose (1994) compared radiative transfer calculations for volcanic ash clouds using different refractive indices (from Pollack et al., 1973; Volz, 1973) and different size distributions (uniform, gamma and log-normal) and found that the size distribution is more important for a mass retrieval than the refractive index, and that BTD_{11-12} is negative for effective radii less than 5 μm but can be positive for larger particles. Also the form of the brightness temperature spectrum is sensitive to the particle size (Gangale et al., 2010). Assuming a log-normal distribution with an uncertainty in the spread (i.e. geometric standard deviations of 1.8 to 2.5) can lead to uncertainties of > 20% in the retrieval of mass column loadings (Western et al., 2015). Newman et al. (2012) compared equal volume spheres (Mie calculation) with randomly oriented hexagonal columns of aspect ratio unity (T-matrix calculation) as volcanic ash particles, and found differences of up to 10% for extinction cross sections in the infrared. Non-spherical rugged vesicular volcanic ash particles were compared with mass-equivalent spheres as well as volume-equivalent spheres with an effective refractive index corrected for the vesicles by Kylling et al. (2014). Although similar for small sizes, significant differences in the optical properties were found for larger particles (e.g. for mass-equivalent radii > 4 μm at the wavelength 12 μm when comparing non-spherical small vesicle particles with volume-equivalent spherical small vesicle particles). The volume-equivalent approach generally modeled reality better.

A limited number of measurements of the refractive indices of volcanic ash exist in the ultraviolet, visible and near-infrared part of the spectrum (Vogel et al., 2017). In the infrared Pollack et al. (1973) presented laboratory measurements of obsidian, basaltic glass and andesite, and Volz (1973) of pumice (all in form of polished rock slabs, KBr or pure pellets). These data sets have been used for decades in volcanic ash retrievals (e.g. Prata, 1989; Wen and Rose, 1994; Prata and Grant, 2001; Yu et al., 2002; Gangale et al., 2010; Pugnaghi et al., 2013; Ishimoto et al., 2016). However, it is known that these retrievals are very sensitive to the refractive index (Wen and Rose, 1994; Western et al., 2015; Prata et al., 2019), and thus an accurate assumption of the refractive index could significantly improve them.

Recent studies have attempted to address this shortcoming: Grainger et al. (2013), Reed et al. (2018) and Deguine et al. (2020) performed laboratory measurements to determine the refractive indices for various volcanic ash samples of different geographical origin, composition and in suspension. Ishimoto et al. (2016) used hyperspectral data collected by satellite and established refractive indices (from Pollack et al., 1973) to constrain the parameters (effective radius, optical depth, cloud pressure height and the volume fraction for a mixture of known refractive indices of volcanic ashes) of multiple volcanic ash clouds. In a second step, those parameters were fixed and the imaginary part of the refractive index was retrieved. Wavelength-dependent

variations up to factors of two or three were found for the refractive index in the infrared, indicating that the accurate knowledge of the refractive index is important.

In case of a future volcanic eruption a consolidated refractive index model together with the necessary, early, rapid chemical or mineralogical analysis of a sample would be sufficient to predict the refractive index of the volcanic ash and increase the performance of the satellite retrievals. To this end, Prata et al. (2019) performed wavelength-dependent linear regressions for both parts of the complex refractive index of volcanic ash with respect to either the silica content x_s or the ratio of non-bridging oxygens to tetrahedrally coordinated cations, using the refractive indices from Reed et al. (2018).

A different approach is to estimate the refractive index for a specific volcanic ash by calculating the corresponding weighted average of the known refractive indices of minerals, glasses and gas bubbles based on their typical abundance in volcanic ashes. It allows the refractive index to be calculated for different compositions and to consider aging processes, e.g. the increase of glass to mineral ratio or the decrease of porosity (Shipley and Sarna-Wojcicki, 1982; Mackie et al., 2016). Thus, a more accurate estimate of the refractive index for an application can be made, and its variability can be investigated by changing the composition within realistic ranges. The impact on the optical properties of the composition in comparison to the microphysics can be analyzed, as has been done for mineral dust (e.g. Hansell Jr. et al., 2011). The uncertainty of retrievals relying on one specific refractive index can be investigated, and it enables to consider the possibility to retrieve the volcanic ash composition remotely. Therefore we use this approach, which was previously implemented for mineral dust in a similar fashion (Sokolik and Toon, 1999; Lee and Park, 2014). For volcanic ash Klüser et al. (2013) achieved good results using a limited set of refractive indices of minerals in remote sensing applications.

The paper is organized as follows: In the methods section (Sec. 2) we describe an approach to determine the refractive indices of volcanic ashes based on their composition, discuss the influence of porosity, the mineral content and a technique to determine the refractive indices of volcanic glasses. We also compile the microphysical properties (size, shape) of volcanic ash particles from literature and outline a simple model to determine BTD_{11-12} . In the results section (Sec. 3) we determine the refractive indices of volcanic glasses and the bulk refractive indices of generic volcanic ashes. Then we quantify the impact of composition and microphysical properties on the optical properties. In the discussions section (Sec. 4) the results are analyzed and the different parameters are ranked regarding their importance for the determination of volcanic ash optical properties. The influence of the composition on the BTD_{11-12} is quantified as an example. Finally, we give a conclusion.

2. Methods

In the following we first describe a procedure to calculate the complex refractive index and the bulk density of different volcanic ashes (Sec. 2.1). Second, we review microphysical properties (size, shape) of volcanic ash particles (Sec. 2.2). Using all these properties we are then able to calculate the optical properties and the brightness temperature difference BTD_{11-12} of volcanic ashes (Sec. 2.3).

2.1. Model for the refractive index and the bulk density of volcanic ash

Generally, volcanic ash particles are created by the fragmentation of volcanic rocks (e.g. due to explosion of small bubbles of exsolved volatiles within a magmatic froth, reaction of hot magma with water in phreatomagmatic eruptions or milling during pyroclastic flows). Therefore they are highly irregular. Magma typically consists of a suspension of silicate melt, large minerals grown slowly in deep magma reservoirs (phenocrysts), small minerals grown during magma ascent (microlites) and exsolved bubbles. After fragmentation, volcanic ash particles

represent fragments containing these components in different proportions, with the silicate melt quenched to a volcanic glass, as well as lithic material collected during the eruption (Langmann, 2013; Jerram and Petford, 2011; Sen, 2014). The latter category is negligible for many eruptions, and is neglected for the purposes of this study. In the following we parameterize the remaining components and combine the individual refractive indices to a single effective refractive index.

2.1.1. Parameterization of the effective refractive index

There are different possible indices available to parameterize the composition of volcanic rocks. In the following we use the silica content x_s (in weight percent, wt.%) of volcanic ashes, which is often determined and regularly used for their classification (Rogers, 2015). It depends on the tectonic location of the individual volcano and the magma genesis conditions, as well as storage, segregation and mixing within a subvolcanic plumbing system prior to eruption (Rogers, 2015; Freundt and Schmincke, 1992). Variations have been determined even within a single eruption event (Gudmundsson et al., 2012).

Other indices have been proposed as well: Prata et al. (2019) investigated the correlation between the refractive index of volcanic ash and the silica content as well as the polymerisation of the melt, defined by the ratio between nonbridging oxygens and tetrahedrally coordinated cations; the latter was favored due to a wider spectral range with coefficients of determination $R^2 > 0.5$. Cooper et al. (2002) showed that the ratio of silica and the amount of oxides of Si, Ca, Fe and Mg was superior to the silica content with respect to the correlation between their index and the position of specific spectral features (Christiansen and transparency feature). As these indices reflect not only the silica present in a rock, but also the abundance of specific elements, they might be able to better represent the chemical and therefore also mineralogical composition.

Aerosols can be mixed internally (each particle consists of multiple components) or externally (each particle consists of a single component which can differ between particles, Lesins et al., 2002). Except for the most silicic compositions consisting only of glass shards, volcanic ash contains both types of mixtures: Crystals surrounded by volcanic glass (Shipley and Sarna-Wojcicki, 1982; Casadevall, 1994) as well as single crystals fragments or glass sherds (Hornby et al., 2019). Following ash emissions, surface brines and salts formed from ash-gas reactions involving sulfur dioxide and other volatiles emitted at the eruption might be possible (Rose, 1977; Langmann, 2013; Casas et al., 2019), but are neglected for simplicity in this work. The volume weighted averaging has been used for external mixtures (Ebert et al., 2002; Ball et al., 2015) as well as internal mixtures (Sokolik and Toon, 1999; Lesins et al., 2002; Lee and Park, 2014) and is therefore used here. Note that other approximations (Bruggeman, Maxwell-Garnet) exist for the calculation of internal mixtures. Although these might lead to different results, there are indications that the impact of the mixing formula is mostly rather small in the infrared (Sokolik and Toon, 1999; Lesins et al., 2002; Lee and Park, 2014).

The complex refractive index of the different components/mixtures is denoted m_x , with n_x the real and k_x the imaginary part. Volume weighted averaging of the components gives the effective refractive indices of the mineral part m_{\min} , of the solid volcanic material m_{volc} including volcanic glass and minerals, and of the volcanic ash mixture m_{eff} including volcanic glass, minerals and voids, Eqs. (2) to (4).

$$m_{\text{eff}} = f_{\text{void}}m_{\text{void}} + (1-f_{\text{void}})m_{\text{volc}} \quad (2)$$

$$m_{\text{volc}} = f_{\text{glass}}m_{\text{glass}} + (1-f_{\text{glass}})m_{\min} \quad (3)$$

$$m_{\min} = \sum_i f_{\min}^i m_{\min}^i \quad (4)$$

f_{void} denotes the volume fraction that is occupied by gas pockets with respect to the volume of a convex hull covering the complete

porous particle, f_{glass} the volume fraction occupied by volcanic glass with respect to the solid volume, and f_{\min}^i the volume fraction of the i^{th} mineral with respect to the crystalline volume. The bulk rock density is calculated similarly.

2.1.2. Porosity

One central driver of volcanic eruptions is the nucleation of gas bubbles due to supersaturation of the magma by volatile elements. These might grow with time and finally burst explosively. For ash particles the volume fraction filled by bubbles can be higher than 80% (Sparks, 1978). However, the actual porosity of the ash particles is size dependent: if the bubble size distribution peaks at sizes smaller than the particle size distribution, a significant amount of gas pockets might be present. But when the original bubbles are larger than the particles, porosity should be negligible, and the particles will contain bubble wall fragments.

Theoretical considerations suggest that the majority of bubbles in volcanic ash should have a size of a few micrometers or larger (Sparks, 1978). Measured bubble sizes in volcanic ash show multiple peaks, indicating multiple bubble nucleation processes (Klug and Cashman, 1994; Genareau et al., 2012, 2013; Colucci et al., 2013). Using backscattered electron images (Klug and Cashman, 1994) and stereo-scanning electron microscopy (Genareau et al., 2012, 2013) bubble size distributions have been shown to typically peak at diameters of 10 to 20 μm , but also at radii of 0.3 μm (Colucci et al., 2013). Using nitrogen gas adsorption Delmelle et al. (2005) concluded that the contribution from bubbles of diameters $< 0.05 \mu\text{m}$ to the porosity is rather negligible; their pore size distributions showed small peaks for 0.005 μm . Mills and Rose (2010) found differences in the surface area estimates of a factor 8 for volcanic ash of size $< 130 \mu\text{m}$ between nitrogen gas adsorption and three-dimensional scanning electron microscope stereo-pair analyses (resolution of 0.01 μm), which they contribute at least partially to the occurrence of microporosity. From in-situ measurements of plumes of degassing volcanoes Shcherbakov et al. (2016) derived for particles with effective diameter of 1.5 to 2.8 μm a porosity of 18 to 35% based on the measured aerosol refractive index. Further work to constrain the effect of microporosity on the refractive index is encouraged, but note that with respect to the total volume occupied by the gas pockets the main contribution comes from bubbles with diameters larger than 10 μm (Genareau et al., 2013; Cioni et al., 2014).

Other factors have an influence on the presence of bubbles as well. For instance a higher silica content connected to a higher viscosity might lead to smaller bubbles and a higher porosity (Genareau et al., 2013). Also the distance from the volcano is an important parameter, as larger and denser particles will sediment faster. Shipley and Sarna-Wojcicki (1982) reported that at distances of 50 km and farther the finest ash consists mainly of glass shards of fragmented porous particles. Also Genareau et al. (2013) showed that for distances farther than 250 km from the eruptive vent/location simple particles (glassy shards without vesicles, diameter $< 30 \mu\text{m}$) contribute the major part to the ash with respect to the mass, whereas more complex particles (larger with multiple imprints of bubbles and probably internal vesicles) contribute less and less. However, in-plume measurements by Rose et al. (1980) showed that in crystal-bearing volcanic ash the smallest fractions consist of crystal fragments.

In this work, we consider mainly particles with radii of a few micrometers. As many measurements indicate that bubbles are of a similar size or larger, we assume no internal bubbles in most parts of this work, i.e. $f_{\text{void}} = 0$. For particles larger than roughly 10 μm , this assumption does not hold. In this case we follow Kylling et al. (2014) and assume $m_{\text{void}} = 1$. Alternatively, pumice (a volcanic glass with a porous texture) as a component (using Volz, 1973) can be considered. The density of vesicles filled with air is significantly lower than typical volcanic ash densities, such that we assume $\rho_{\text{void}} = 0 \text{ g cm}^{-3}$.

2.1.3. Crystals

The presence of typical minerals as well as their relative volume abundance can be related to the silica content according to the distribution in Fig. 3.10 (a classification scheme for igneous rocks) in Jerram and Petford (2011) (see also Rogers, 2015; Sen, 2014; Nakagawa and Ohba, 2002) for typical silica contents x_s , Eq. (5).

$$x_s \in \{45, 50, 55, 60, 65, 70, 75\} \text{ wt.}\% \quad (5)$$

The corresponding volume fractions with respect to the bulk silica content are given in Table 1. In reality the composition might slightly deviate from the distribution in Table 1. Therefore, instead of directly applying Eq. (4), we use these fractions f_{\min}^i as mean values, assuming a certain variability in the composition. We add a random normally distributed value (mean of 0, width of 0.2) to each fraction f_{\min}^i , set resulting negative values to zero and normalize the distribution. Using Eq. (4) with this new phase distribution gives us m'_{\min} . The mean of m'_{\min} , \bar{m}_{\min} , is determined by repeating the calculation N times and averaging the results. $N = 10000$ was found to be sufficient to get the maximum of the wavelength-dependent standard deviation of the real and imaginary part of \bar{m}_{\min} being < 0.03 . \bar{m}_{\min} and a similarly calculated density are used from now on; for simplicity we drop the bar. Note that for the refractive index a slightly different composition is used than for the density, as corresponding data for amphibole are lacking. Thus, the relative composition for the refractive index is calculated by dropping amphibole prior to normalization.

The mineral phase distribution of Jerram and Petford (2011) included potassium feldspar, plagioclase and pyroxene. The first is here represented by orthoclase. The type of plagioclase changes depending on the silica content, being sodium-rich for felsic and calcium-rich for mafic ashes (Jerram and Petford, 2011). Therefore we use albite, labradorite and anorthite to represent this behavior. For $x_s = 75$ wt.% the plagioclase is assumed to consist only of albite, for $x_s = 54$ wt.% of labradorite and for $x_s = 40$ wt.% of anorthite. In between we apply a linear interpolation and use a mixture of two minerals. The composition of labradorite equals on average 40% (30 to 50%) albite and 60% (50 to 70%) anorthite (Ralph, 2020a). The pyroxene is assumed to contain orthopyroxenes (here enstatite) and clinopyroxenes (here diopside) in equal parts. Furthermore, quartz, muscovite, biotite, amphibole and olivine are used.

Note that we assume that the minerals with the largest contribution with respect to the crystalline volume also lead to the major contributions to the refractive index and the density. However, there are minor components with respect to the volume, that might still be able to have non-negligible influence (Best, 2003). Magnetite for instance,

an iron-oxide, has a much higher density than most other components as well as a different refractive index, see Table 2 and Fig. 1. Therefore, we assume that 1 vol.% of the ash consists of magnetite as a representative of all iron- and titanium oxides (already included in Table 1).

The wavelength dependence of the real and imaginary part of the minerals in Table 1 (taken from different sources, see Table 2) is shown in Fig. 1. Various refractive indices are calculated using dispersion analysis as described in the corresponding papers (anorthite, clinopyroxene, muscovite, labradorite, obsidian, olivine, orthoclase, orthopyroxene). Cases where multiple indices were given for the different orientations of the crystal with respect to the electromagnetic field or measurement techniques are averaged assuming equal weighting (biotite, muscovite, labradorite, obsidian, orthoclase). For quartz the ordinary and the extraordinary ray are mixed 2:1 (Peterson and Weinman, 1969). This corresponds to the assumption of random orientation of the particles. Also note that some materials were glassy (albite). For small wavelengths ($< 7 \mu\text{m}$) we assume a constant refractive index $m = 1.4 + 0 \cdot i$ if missing.

The wavelength dependence of the component refractive indices already shows some noteworthy features. Fig. 1 (g, h) shows the minerals typical for felsic rocks, while Fig. 1 (c, d) shows minerals of mafic rocks. The peaks of the imaginary part of the felsic minerals are slightly shifted towards smaller wavelengths with respect to the mafic minerals, Fig. 1 (h, d). Similarly, the steep rise of the real part is shifted to smaller wavelengths for felsic minerals compared to the mafic minerals, Fig. 1 (g, c). Crystalline quartz has a significantly higher peak in the imaginary part than all other minerals, Fig. 1 (g). Note that diopside shows besides its own characteristic features also peaks at the same wavelengths as quartz, Fig. 1 (c, d). Fig. 1 (a, b) shows volcanic glasses for comparison: they exhibit the same tendencies and features as the crystals (except for magnetite) but with peaks at different wavelengths and they appear smoother. Magnetite has a completely different refractive index than all other components for 5 to 15 μm without prominent features, Fig. 1 (e, f); they appear for larger wavelengths (16 to 50 μm) instead (Glotch and Rossman, 2009).

The densities are taken from other sources than the refractive indices, see Table 2, and therefore might correspond to slightly different samples. For instance the refractive index used for albite is taken from Mutschke et al. (1998). However, their sample was in the glass state and had a density of only 2.36 g cm^{-3} . As we want to approximate crystals, we assume a higher density of $2.625 \pm 0.025 \text{ g cm}^{-3}$ corresponding to crystalline albite (Ralph, 2020b). In many cases an interval of possible densities was given. Then we use the mean and half of the width as the uncertainty.

2.1.4. Glasses

For felsic compositions volcanic ash often consists mostly of glassy particles and only to a minor fraction of minerals. Thus, the glass volume fraction f_{glass} is often rather high. Vogel et al. (2017) showed that the glass fraction (analyzed from the areas of glass and minerals in two-dimensional images of ash particles) is proportional to the silica content x_s . During its lifetime f_{glass} might increase even more due to sedimentation of the crystals, which have a higher density and a less rugged surface than the glass shards (Shipley and Sarna-Wojcicki, 1982; Mackie et al., 2016). This can lead to glass fractions of up to 1 (Heiken, 1974; Rose et al., 2003).

Measurements of the refractive index and the silica content of various volcanic glasses have been performed by Pollack et al. (1973). However, the silica content of the glass might be considerably higher than the silica content of the bulk magma as a result of the crystals (except quartz) being less silicic than the bulk material. Therefore, an increase in crystallization increases the difference in silica content between glass and bulk, up to 10 wt.% (Mackie et al., 2016). In addition, Reubi and Blundy (2009) showed that melt inclusions (i.e. melt trapped in phenocrysts) have a bimodal compositional distribution with a significant absence of intermediate compositions (i.e. 59 to 66 wt.%), although

Table 1

Rounded volume fractions f_{\min}^i of mineral phases in volcanic ash with respect to the crystalline part according to Fig. 3.10 in Jerram and Petford (2011) for different bulk silica contents. The minerals are orthoclase (OC), quartz (Q), albite (AL), labradorite (L), anorthite (AN), enstatite (E), diopside (D), olivine (OL), muscovite (MU), biotite (B), amphibole (AM) and magnetite (MA). See text for further explanation.

Mineral	Silica content x_s / wt.%						
	45	50	55	60	65	70	75
OC	0.00	0.00	0.01	0.06	0.12	0.22	0.45
Q	0.00	0.00	0.06	0.13	0.23	0.33	0.23
AL	0.00	0.00	0.02	0.13	0.17	0.13	0.13
L	0.08	0.27	0.49	0.34	0.15	0.04	0.00
AN	0.15	0.11	0.00	0.00	0.00	0.00	0.00
E	0.29	0.29	0.09	0.00	0.00	0.00	0.00
D	0.29	0.29	0.09	0.00	0.00	0.00	0.00
OL	0.17	0.02	0.00	0.00	0.00	0.00	0.00
MU	0.00	0.00	0.00	0.00	0.00	0.08	0.13
B	0.00	0.00	0.05	0.12	0.14	0.08	0.04
AM	0.00	0.00	0.16	0.21	0.18	0.10	0.00
MA	0.01	0.01	0.01	0.01	0.01	0.01	0.01

Table 2
Literature sources for the refractive indices at the given wavelengths λ and their densities ρ .

Component	Refractive Index Source	$\lambda / \mu\text{m}$	Remark to sample/meas.	Density Source	$\rho / \text{g cm}^{-3}$
Quartz glass (SiO ₂ 100 wt.%)	Kitamura et al. (2007)	0.21 to 50	combination of different measurements	Wakaki et al. (2007)	2.202 ± 0.001
Obsidian (SiO ₂ 75 wt.%)	Koike et al. (1989)	2.5 to 400	KBr pellet (transmission), slab of bulk (reflection)	Clark (1966)	2.37 ± 0.04
Basaltic glass (SiO ₂ 53.45 wt.%)	Pollack et al. (1973)	0.2 to 50	slab of bulk (reflection)	Clark (1966)	2.78 ± 0.07
Orthoclase	Arnold et al. (2014)	2.5 to 40	slab of crystalline material (reflection)	Best (2003)	2.59 ± 0.04
Quartz	Spitzer and Kleinman (1961), Peterson and Weinman (1969)	0.768 to 37	slabs of crystalline material (reflection, transmission)	(Best, 2003)	2.65 ± 0.01
Albite (Plagioclase)	Mutschke et al. (1998)	6.7 to 500	slabs of glassy material (reflection)	Ralph (2020b)	2.625 ± 0.025
Labradorite (Plagioclase)	Ye et al. (2019)	5 to 44.4	slab of crystalline material (reflection)	0.6 $\rho_{\text{anorthite}}$ + 0.4 ρ_{albite} (Ralph, 2020a)	2.70 ± 0.05
Anorthite (Plagioclase)	Aronson and Strong (1975)	6.25 to 40	slab of crystalline material (reflection)	Ralph (2020c)	2.75 ± 0.01
Enstatite (Orthopyroxene)	Roush et al. (1991)	5 to 25	KBr pellet (reflection)	Best (2003)	3.55 ± 0.35
Diopside (Clinopyroxene)	Aronson and Strong (1975),	5.88 to 43.48	slab of crystalline material (reflection)	Best (2003)	3.35 ± 0.15
Olivine	Mukai and Koike (1990)	72 to 200	KBr pellet (transmission)	Best (2003)	3.8 ± 0.6
Muscovite	Aronson and Strong (1975), Vedder (1964)	6.67 to 31.25	slab of crystalline material (reflection)	Ralph (2020d)	2.825 ± 0.055
Biotite	Querry (1983)	0.25 to 55.56	slab of crystalline material (reflection)	Haldar and Tišljarić (2014)	3.05 ± 0.35
Amphibole (Hornblende)	NA	NA	NA	Best (2003)	3.275 ± 0.225
Magnetite	Glotch and Rossman (2009)	5 to 100	slab of crystalline material (reflection)	Ralph (2020e)	5.175 ± 0.001

they are widespread. They proposed that intermediate compositions might be created by magma mixing, and therefore contain volcanic glasses with a silica content up to about 15 wt.% higher.

To circumvent this problem the refractive indices of volcanic glasses are derived from bulk ash samples, for which the bulk silica content is known. We invert Eqs. (2) to (4) to obtain m_{glass} from m_{eff} , i.e. the bulk refractive index, by making assumptions on the remaining

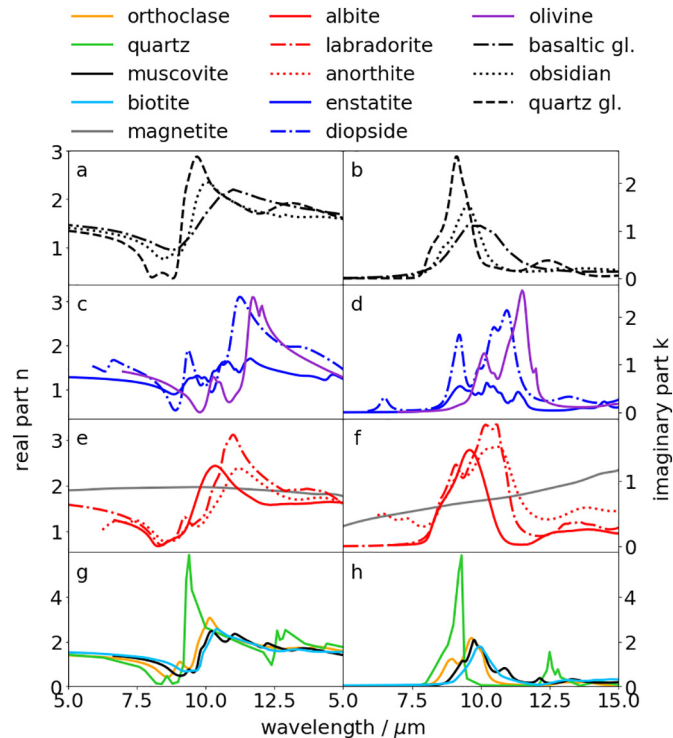


Fig. 1. Wavelength dependence of the real and imaginary part of the refractive index of the minerals and glasses in use.

quantities (f_{void} , m_{void} , f_{glass} and m_{min} , see details below). The refractive indices of bulk volcanic ash samples are taken from Reed et al. (2018) and Deguine et al. (2020), who investigated samples of seven (Grímsvötn 2011, Aso 1993, Eyjafjallajökull 2010, Tongariro 2012, Spurr 1992, Nisyros, Askja 1875) and six (Etna 2017, Grímsvötn 2011, Calbuco 2015, Eyjafjallajökull 2010, Puyehue-Cordón Caulle 2011, Chaitén 2008) different volcanic eruptions, respectively. The samples cover silica contents x_s from 49.1 to 70.7 wt.% and 46.5 to 74.1 wt.%, respectively; x_s of the Spurr sample was not given, and therefore is taken from Vogel et al. (2017). The particle diameter are mostly < 3 μm . The silica contents were determined by X-ray fluorescence analysis and the refractive indices from the extinction spectra of volcanic ash suspended in nitrogen in the infrared to ultraviolet spectrum. The densities were given neither by Reed et al. (2018) nor by Deguine et al. (2020); thus, we use the linear relation by Vogel et al. (2017) to calculate the bulk dense rock equivalent density of volcanic ash from the silica content; an uncertainty of 0.1 g cm^{-3} is assumed. As the particles are small we assume that porosity is negligible, i.e. $f_{\text{void}} = 0$ (therefore, m_{void} is not needed). For the glass $f_{\text{glass}} = x_s/100 \text{ wt.}\% \pm 0.05$ is chosen (Vogel et al., 2017). The mineral composition is based on the rounded x_s (to 45, 50, 55 wt.% etc., see Table 1); the uncertainty is set to 2.5 wt.%. The potential impact of the adjusted parameters is demonstrated with an example, then m_{glass} is calculated using the assumptions. Negative values are set to zero.

We combine our volcanic glass calculations with the laboratory measurements of basaltic glass, obsidian and quartz, see Table 2. For basaltic glass the silica content ($x_s = 53.45 \text{ wt.}\%$) was given by Pollack et al. (1973). For obsidian the silica content was not given, but the refractive index is similar to the obsidian refractive index in Pollack et al. (1973), with values around $x_s = 75 \text{ wt.}\%$. Quartz glass as a pure silicate glass (i.e. $x_s = 100 \text{ wt.}\%$) does not appear as a volcanic glass in nature. However, as the volcanic glasses from mafic to felsic have an increasing silica content, quartz glass can be considered as an extrapolation of this regime. Note that for basaltic glass and obsidian we ignore the possible difference between bulk and glass silica content. The refractive indices of the glasses, Fig. 1, show a similar behavior as the minerals with respect to the silica content, but the peaks are generally smaller and overall smoother.

In the next step we follow Prata et al. (2019) and perform separately a wavelength-dependent linear regression for the real (n) and

imaginary part (k) of the refractive index of volcanic glass, using x_s as the independent variable. For instance the peak of k shifts towards smaller wavelength with increasing x_s for volcanic glasses (see Sec. 2.1.3). Therefore, it is possible that for a specific wavelength k first increases, reaches a maximum, and then decreases again. Thus, we assume for the fit a quadratic function, Eq. (6).

$$g_i = a_i + b_i x_s + c_i x_s^2 \quad (6)$$

g_i is n or k of volcanic glass at a wavelength i , and a_i , b_i , c_i are the corresponding fit coefficients. Finally, we use these functions to calculate the real and the imaginary part of the refractive index of volcanic glasses from 45 to 100 wt.% with the corresponding 1σ prediction band. Again, occasional negative values are set to zero. Similarly, we calculate the density, only using a linear instead of a quadratic function.

2.2. Microphysical properties of volcanic ash

Next we compile typical sizes and shapes of volcanic ash in order to quantify the impact of these microphysical properties on the optical properties of volcanic ash. Then we compare these impacts with the effects of the composition in order to select parameters for the determination of a representative set of optical properties.

2.2.1. Size distribution of volcanic ash particles

First, we select the type of size distribution for volcanic ash particles. The Weibull distribution has been reported from measurements (Stevenson et al., 2015), in addition the modified gamma distribution (Prata, 1989; Prata and Grant, 2001; Gangale et al., 2010) or more often the log-normal distribution (Farlow et al., 1981; Prata, 1989; Prata and Grant, 2001; Yu et al., 2002; Gangale et al., 2010; Grainger et al., 2013; Lee et al., 2014; Stevenson et al., 2015) has been used to characterize volcanic ash particles. Also multi-modal distributions have been reported (e.g. Wohletz et al., 1989; Riley et al., 2003). As the size of volcanic tephra varies over a large regime, we use log-normal distributions (Limpert et al., 2001) described by Eq. (7).

$$n(r) = \frac{N_0 \exp\left[-\frac{1}{2} \left(\frac{\ln(r) - \ln(r_m)}{\ln(s)}\right)^2\right]}{\sqrt{2\pi} \ln(s) r} \quad (7)$$

N_0 denotes the total particle number density, r the radius (see also Sec. 2.2.2 for non-spherical particles), r_m the median and s the geometric standard deviation parameterizing the width of the distribution. The effective radius r_{eff} , defined as the quotient of the third to the second moment of $n(r)$, becomes Eq. (8).

$$r_{\text{eff}} = r_m \exp\left(\frac{5}{2} \ln(s)^2\right) \quad (8)$$

With respect to remote sensing applications, we are interested in fine ash particles and consider $r_{\text{eff}} \in \{0.6, 1.8, 3, 4.5, 6\} \mu\text{m}$. This regime has been investigated in the laboratory (Reed et al., 2018; Deguine et al., 2020), in-situ (Rose et al., 1980; Schumann et al., 2011) and in many remote sensing applications (Pugnaghi et al., 2013; Grainger et al., 2013; Ishimoto et al., 2016). However, there is some unsolved discrepancy between the typical sizes in air- and spaceborne investigations and those found for cryptotephra. The latter shows systematically higher values, e.g. median number diameters (i.e. long axis length as used in the field of cryptotephra) of 20 to 70 μm at distances of about 1000 km (Stevenson et al., 2015) or mode diameters (average of 64 diameters) for mass density distributions of 90 μm at 1400 km (Rose et al., 2003). These variations might arise from differences in the measuring techniques and their sensitivities (Stevenson et al., 2015). Theoretically, considering only sedimentation for spherical ash particles, those larger particles are expected to fall out of the atmosphere fast, e.g. particles

with radii around 20 μm should stay in the troposphere less than one day, whereas particles with radii of 1 μm might remain up to months (Grainger et al., 2013). However, as volcanic ash particles are not spherical but sometimes highly irregular, their terminal velocity might be significantly lower, and therefore their atmospheric residence time could be longer (Rose et al., 2003; Riley et al., 2003).

Typical values for the spread s in Eq. (7) are 1.53 to 1.74 (for ash from Mt. St. Helens, Farlow et al., 1981), 2.1 (for ash from Mt. Redoubt, Wen and Rose, 1994), 1.38 to 1.66 (from cryptotephra, Stevenson et al., 2015) or 1.5 to 1.77 (applied in Grainger et al., 2013). Thus, we consider $s \in \{1.5, 2.0\}$ in the following analysis.

2.2.2. Shape of volcanic ash particles

Second, we consider the shape of volcanic ash particles. These usually have a very rugged surface. However, for simplicity we confine our analysis to spheres and pro- and oblate spheroids. Kylling et al. (2014) showed that the differences in optical properties between non-spherical rugged vesicular volcanic ash particles and volume-equivalent spheres with an effective refractive index corrected for the vesicles is small for the sizes considered here. For larger particles these differences as well as the variability between different realistic particle shapes increases.

Typical aspect ratios of volcanic ash are 1.4 (Vogel et al., 2017), 1.38 to 1.81 (Ball et al., 2015), 1.8 to 2.2 (Schumann et al., 2011), 1.4 to 2.5 (Riley et al., 2003). Vogel et al. (2017) suggest that the aspect ratio decreases to 1.25 to 1.3 for radii smaller than 5 μm . The density distribution with respect to the aspect ratio can be parameterized by a modified log-normal distribution, Eq. (9) (Gasteiger and Wiegner, 2018).

$$n(\varepsilon) = \frac{\exp\left[-\frac{1}{2} \left(\frac{\ln(\varepsilon-1) - \ln(\varepsilon_0-1)}{\sigma_{\text{ar}}}\right)^2\right]}{\sqrt{2\pi} \sigma_{\text{ar}} (\varepsilon-1)} \quad (9)$$

ε denotes the aspect ratio, ε_0 its median and σ_{ar} the spread. Kandler et al. (2007) described Saharan dust by Eq. (9) with $\varepsilon_0 = 1.64$ and $\sigma_{\text{ar}} = 0.66$. To show that the same distribution can be used for volcanic ash we apply it to the aspect ratio distribution of two Sakurajima samples from Miwa et al. (2015), Fig. 2. Fitting yields $\varepsilon_0 = 1.7$ and $\sigma_{\text{ar}} = 0.45$. Thus, we consider $\varepsilon_0 \in \{1.5, 2.0\}$ and $\sigma_{\text{ar}} \in \{0.45, 0.66\}$ in the following analysis.

The definition of a radius is ambiguous for non-spherical particles. We consider the cross-section-equivalent radius in our study (except when stated otherwise), Eq. (10).

$$r_c = \sqrt{\frac{C_{\text{geo}}}{\pi}} \quad (10)$$

C_{geo} denotes the orientation-averaged cross section of the particles (Gasteiger and Wiegner, 2018). Other definitions of the radius, e.g. via the volume (r_v) or the volume to cross-section ratio (r_{vcr}), are given in Gasteiger and Wiegner (2018). As these different definitions result in different values for the radius for the same particle, and as the size

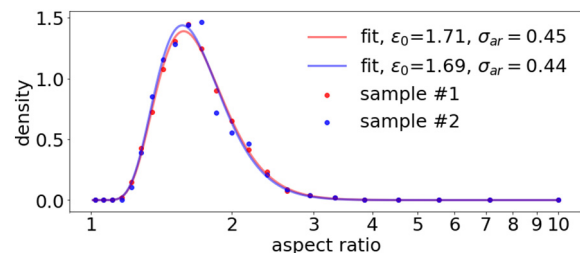


Fig. 2. Fit of the modified log-normal distribution to the aspect ratio distribution given by Miwa et al. (2015).

distribution has a large impact on the optical properties (as will be shown in Sec. 3.2), the radius definition may introduce a significant uncertainty in the optical properties. Gasteiger and Wiegner (2018) pointed out that the appropriate choice depends on the measurement technique applied to determine the size distribution. However, we combine literature values from different measurement techniques. Thus, the influence of the radius definition on the optical properties is investigated in a sensitivity study.

2.3. Optical properties of volcanic ash and a simplified model for BTD_{11-12}

The composition (i.e. refractive index) and the microphysical properties are used to calculate the optical properties (mass extinction coefficient, single scattering albedo and asymmetry parameter). To calculate these properties we use the tool *MOPSMAP* version 1.0 (Gasteiger and Wiegner, 2018). It comprises a precalculated data set of optical properties for single particles in random orientation, using Mie theory for spheres and the T-matrix method for spheroids. Then *MOPSMAP* computes the optical properties for a given ensemble of different single particles by averaging their properties. The input consists of the particle size and shape distribution, the refractive index and the bulk density. Wavelengths between 5 and 15 μm are considered at a resolution of 0.1 μm .

Using the optical properties one can calculate the brightness temperature difference BTD_{11-12} as measured from satellite. Here we adapt a simple model of a single homogeneous volcanic ash layer as described by Prata and Grant (2001) (and applied in Prata and Prata, 2012; Prata et al., 2019). Only two wavelengths (11 and 12 μm) at nadir are considered and scattering effects are neglected. For these wavelengths surface emissivities range roughly between 0.95 and 1, depending on the surface type and the exact wavelength (Zhou et al., 2013). However, for simplicity we assume that the Earth's surface behaves like a black body and that the atmosphere is transparent except for the ash cloud; thus, we obtain Eqs. (11) and (12).

$$I_{11} = (1-t_{11}) B_{11}(T_c) + t_{11} B_{11}(T_s) \quad (11)$$

$$I_{12} = (1-t_{12}) B_{12}(T_c) + t_{12} B_{12}(T_s) \quad (12)$$

Here I_λ denotes the spectral radiance measured at the top of the atmosphere, B_λ the Planck function, T_s and T_c the temperatures of the Earth's surface and the cloud top, respectively. $t_\lambda = \exp(-\beta_\lambda \rho L)$ is the transmissivity with the mass extinction coefficient β_λ , the mass concentration ρ and the geometrical cloud thickness L . We consider a test case with typical values of $L = 1000$ m and $\rho = 0.5$ mg m^{-3} (e.g. Schumann et al., 2011), $T_s = 290$ K and $T_c = 220$ K (about 10 km).

3. Results

3.1. Refractive indices

To begin we consider the potential impact of the parameters f_{glass} , f_{void} and x_s on the derivation of volcanic glass refractive indices. Fig. 3 shows example calculations for the refractive index of volcanic glass derived from the bulk refractive index of Eyjafjallajökull ash by Deguine et al., 2020, which lies with 58.6 wt.% in the center of the regime of typical silica contents. The corresponding densities are given in Table 3. A reference calculation is shown ($f_{\text{glass}} = 0.59$, $f_{\text{void}} = 0$, $x_s = 60$ wt.%) and the results for different variations of the reference settings. A change of f_{glass} by $\pm 0.05\%$ leads only to minor changes of the volcanic glass refractive index and density. However, for the extreme case $f_{\text{glass}} = 1$ the imaginary part of the refractive index increases partly by up to 0.5 and the density by 7%. The variation of x_s by ± 5 wt.% can lead to changes of the refractive index up to about ± 0.2 , whereas the change in the density is of the order of 1%. f_{void} has the largest impact:

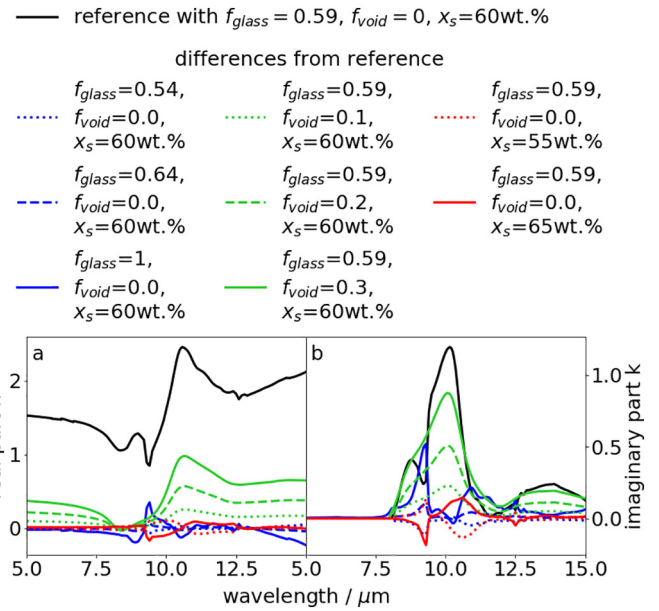


Fig. 3. Wavelength dependence of the real and imaginary part of the refractive index of volcanic glass derived from the bulk refractive index of Eyjafjallajökull ash by Deguine et al., 2020; a reference value is given (black), whereas for the other settings the reference is subtracted, i.e. the difference with respect to this reference is shown (blue, green, red); the parameters f_{glass} , f_{void} and x_s are varied.

Table 3

Density of volcanic glass derived from the bulk properties of Eyjafjallajökull ash by Deguine et al. (2020), varying the parameters f_{glass} , f_{void} and x_s ; the reference calculation is given in the first line, for the other settings the relative deviation of the density with respect to the reference density is given as well.

x_s / wt.%	f_{glass}	f_{void}	ρ_{glass} / g cm^{-3}	
60	0.59	0.00	2.61	(ref.)
60	0.54	0.00	2.56	(-2%)
60	0.64	0.00	2.64	(1%)
60	1.00	0.00	2.79	(7%)
60	0.59	0.10	3.14	(20%)
60	0.59	0.20	3.80	(46%)
60	0.59	0.30	4.65	(78%)
55	0.59	0.00	2.59	(-1%)
65	0.59	0.00	2.61	(0%)

for $f_{\text{void}} = 0.3$ the real part of the refractive index increases by up to 1 and the imaginary part by about 0.8; also the density exhibits an increase of close to 80%.

Next the refractive indices for volcanic glasses calculated from all measurements of bulk volcanic ashes by Reed et al. (2018) and Deguine et al. (2020) are considered in Figs. 4 and 5, respectively; the latter are extrapolated from 14.49 μm up to 15 μm . Also shown are the refractive indices for obsidian, basaltic and quartz glass. Noteworthy are the dips between 9 and 10 μm for both n and k in the calculated refractive indices, Figs. 4 (a, b) and 5 (a, b). For the felsic cases this is probably due to the high peaks of crystalline quartz, whereas for the mafic cases a similar (although weaker) peak was visible in the diopside sample, Fig. 1. Interestingly, these dips are present for the measured volcanic glass refractive indices, such that these exhibit more features than the smoother bulk refractive indices (Reed et al., 2018; Deguine et al., 2020). In Fig. 4 (b) the imaginary part of the refractive index becomes negative for the samples of Aso and Tongario for wavelengths of 10 to 12 μm , and therefore is set to zero here. Similarly, the imaginary parts of some refractive indices are set to zero for wavelengths < 8 μm , Figs. 4 (b) and 5 (b).

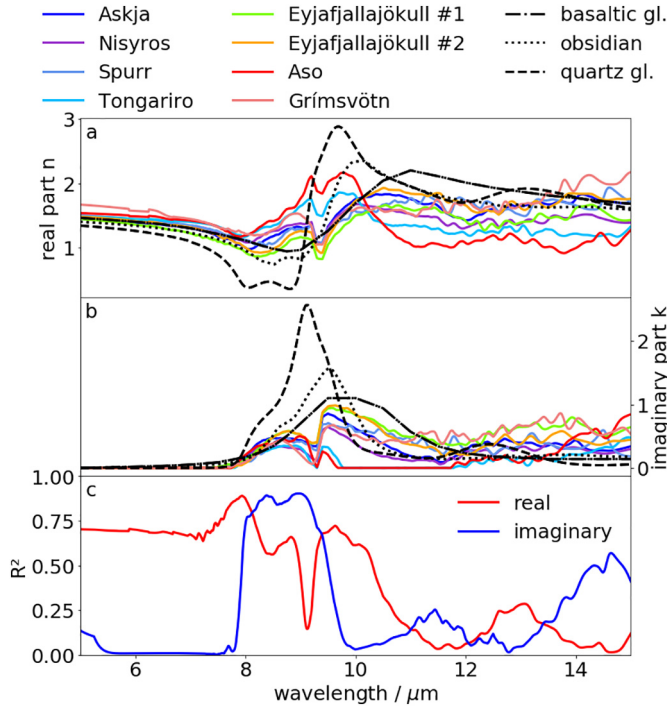


Fig. 4. Wavelength dependence of the real (a) and imaginary part (b) of the refractive indices of the volcanic glasses calculated from refractive indices of Reed et al. (2018) for bulk volcanic ash samples of different volcanos; (c) shows the corresponding R^2 value for the linear regression result at each wavelength.

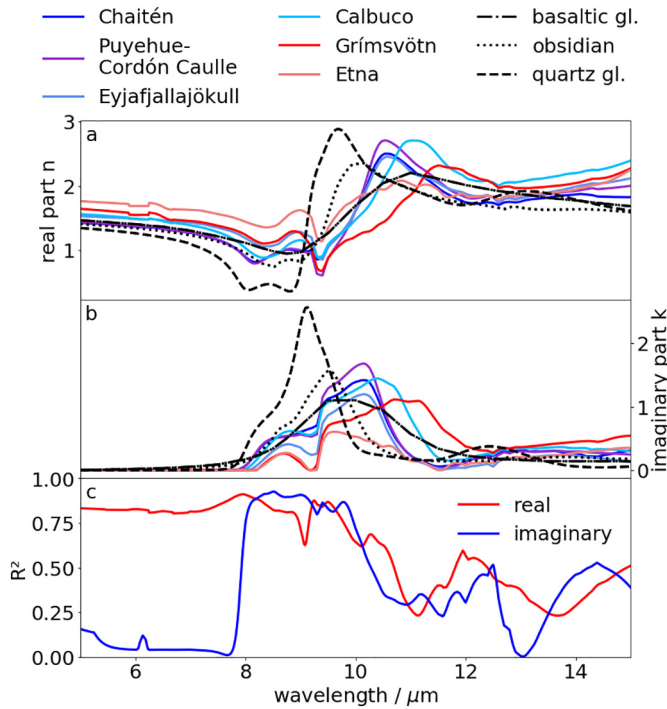


Fig. 5. As Fig. 4 but using refractive indices of Deguine et al. (2020).

Figs. 4 (c) and 5 (c) show the coefficient of determination R^2 for the wavelength-dependent linear regression. A perfect fit results in $R^2 = 1$, whereas a constant fit function returning the mean leads to $R^2 = 0$. The

latter might happen if there is no clear functional dependence between the refractive index and the silica content. In Fig. 4 (c) R^2 of the real part is mostly around 0.7 up to 10 μm , except for a dip between 9 μm and 9.5 μm . Between 11 μm and 15 μm it is mostly < 0.25 ; this is because of the missing quadratic relationship between the refractive index and the silica content (e.g. the real parts of the volcanic glasses of Nisyros and Tongariro are between those of Grímsvötn and Aso, although the last two both have lower silica contents than the first two). For the imaginary part R^2 is roughly zero up to 8 μm as the imaginary parts of the volcanic glasses are mostly zero (or are set to zero if they become negative). R^2 rises to values of approximately 0.8 at wavelengths of 8 to 9.5 μm . Beyond that it remains < 0.25 up to roughly 13.5 μm ; this might be partly due to the vanishing imaginary parts of the refractive indices of the volcanic glasses of Aso and Tongariro. Fig. 5 (c) shows similar values for R^2 as Fig. 4 (c) up to 9.5 μm . Beyond that R^2 decreases for the real and imaginary part to values mostly between 0.25 and 0.5, except for a dip of R^2 of the imaginary part to zero at 13 μm , where the imaginary part of quartz glass intersects all other imaginary parts. Calculating the average R^2 of the real and imaginary part between 8 μm and 12 μm gives 0.41 and 0.4 using Reed et al. (2018), and 0.64 and 0.62 using Deguine et al. (2020). This shows that the linear regression performs significantly better using the data of Deguine et al. (2020) compared to Reed et al. (2018). Therefore, we will use only the data derived from Deguine et al. (2020) from now on. In the next step we use the linear regression results to calculate the wavelength dependence of the refractive indices of volcanic glasses for bulk silica contents x_s between 45 and 100 wt.%, Fig. 6. Fig. 7 shows the calculated glass densities. The linear regression yields $R^2 = 0.88$.

Mathematically n and k are connected by the Kramers-Kronig relation (Lucarini et al., 2005). Its singly subtractive version is given as Eq. (13).

$$\frac{n(\omega) - n(\omega_a)}{\omega^2 - \omega_a^2} = \frac{2}{\pi} \mathcal{P} \int_0^\infty \frac{\bar{\omega} k(\bar{\omega})}{(\bar{\omega}^2 - \omega^2)(\bar{\omega}^2 - \omega_a^2)} d\bar{\omega} \quad (13)$$

ω and ω_a are two wavenumbers and \mathcal{P} denotes the Cauchy principal value of the integral. To check the consistency of the retrieved volcanic glass refractive indices we evaluate if the Kramers-Kronig relation is still fulfilled (Deguine et al. (2020) used a similar approach to determine the real parts of the refractive indices). We extend the imaginary part k of the refractive index assuming $k \propto \lambda^{-1}$ for wavelengths $\lambda > 15 \mu\text{m}$ and $k \propto \lambda^3$ for $\lambda < 5 \mu\text{m}$ (Herbin et al., 2017). The choice of the anchor point $n(\omega_a)$ is crucial for the method (Herbin et al., 2017); we choose $\omega_a = 1000 \text{ cm}^{-1}$ such that the integrand in Eq. (13) becomes largest in the center of the considered spectral regime where also the main

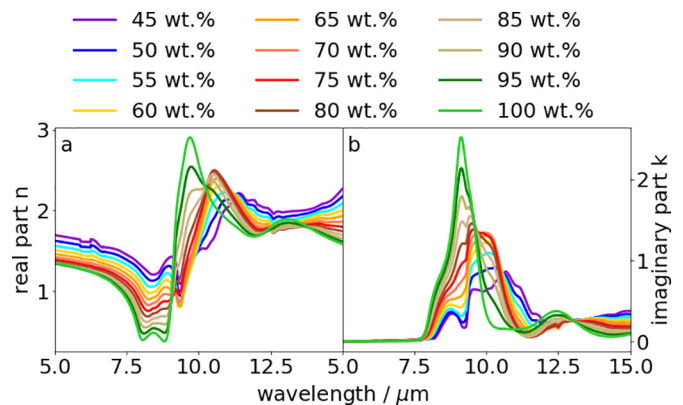


Fig. 6. Wavelength dependence of the real and imaginary part of the refractive indices of the volcanic glasses calculated from the linear regression results for different bulk silica contents.

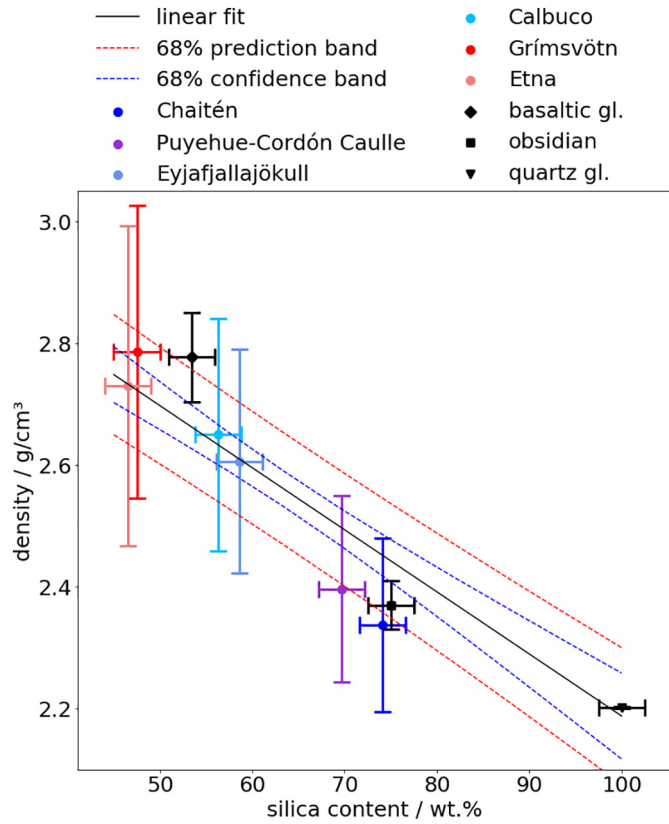


Fig. 7. Density of the volcanic glasses calculated from the bulk samples of different silica contents, typical densities for basaltic, obsidian and quartz glass, and the linear fit for these data.

absorption feature is located, Fig. 5 (b). $n(\omega_a)$ is taken from the individual regression results. The relative deviation of n by Kramers-Kronig and linear regression relative to the latter is up to $\pm 10\%$ for 5 to 14 μm . For wavelengths $> 10 \mu\text{m}$ the deviation increases for larger wavelengths and lower silica contents. At 15 μm the deviation for $x_s = 45 \text{ wt.}\%$ is -17% . Note that this might be at least partially connected to the fact that an assumption was used for k for wavelengths $> 15 \mu\text{m}$ instead of real measurements.

Next we can calculate the refractive indices for different mixtures of volcanic glasses, minerals and bubbles, Fig. 8. We vary different parameters within realistic ranges in order to investigate their impact on the refractive indices of volcanic ashes, i.e. x_s from 45 to 75 wt.%, f_{glass} from $x_s/100 \text{ wt.}\%$ to 1 and f_{void} from 0 to 0.75. In pink, the refractive index for $f_{\text{glass}} = 0$ is shown, i.e. the pure mineral case. The grey shaded area shows the 68% prediction band for the pure volcanic glass case, i.e. for $f_{\text{glass}} = 1$ and $f_{\text{void}} = 0$. This band shows a significant spread, which in many cases is of the same order or even larger than the variability due to minerals.

3.2. Optical properties

Next we quantify the impact of the different microphysical properties and the composition on the optical properties. The largest spread and the corresponding wavelength are given for each property in Table 4. Considering the size distributions described in Sec. 2.2.1 (limited within MOPSMAP to $r \in [0.001, 30] \mu\text{m}$) for spherical particles and using the refractive index of Eyjafjallajökull ash of Deguine et al. (2020) and a density of 2.79 g cm^{-3} (calculated from the silica content and the linear relation of Vogel et al., 2017) we obtain the optical properties shown in Fig. 9. r_{eff} as well as s have a great influence on the optical properties, with r_{eff} dominating over s . The single scattering albedo,

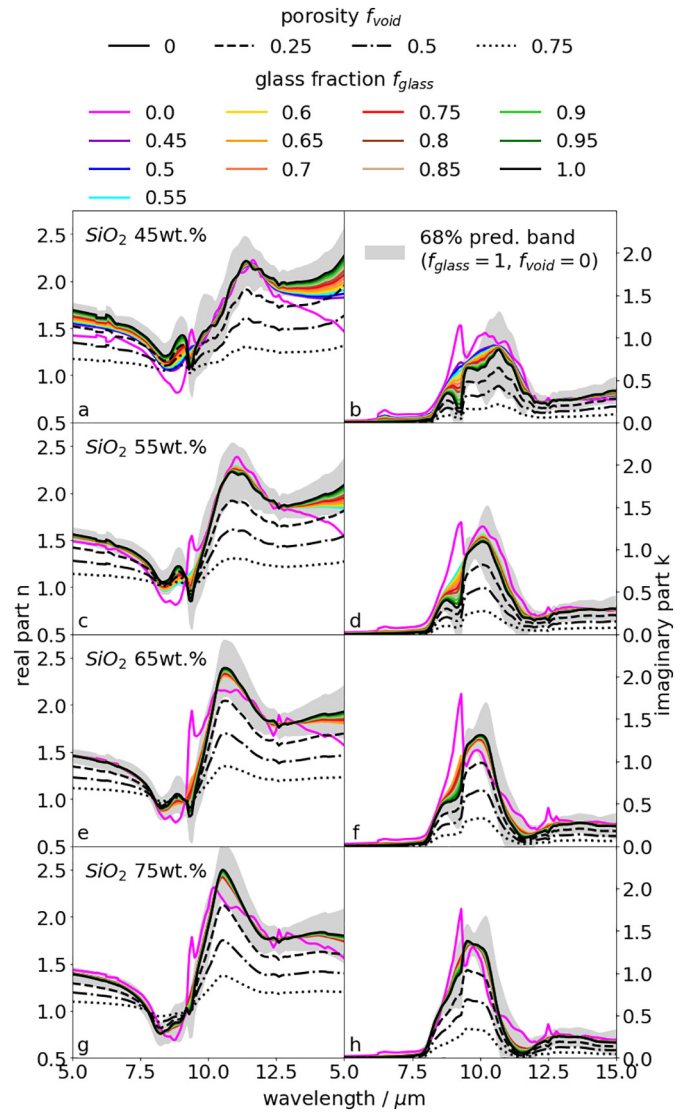


Fig. 8. Wavelength dependence of the real and imaginary part of the refractive indices of volcanic ash mixtures of glasses, minerals and voids with different compositions. f_{glass} is indicated by the color, f_{void} by the linestyle. x_s has values of 45 wt.% (a, b), 55 wt.% (c, d), 65 wt.% (e, f) and 75 wt.% (g, h). Grey shaded is the 68% prediction band for the pure volcanic glass, i.e. for $f_{\text{glass}} = 1$ and $f_{\text{void}} = 0$.

Fig. 9 (b), shows that for small r_{eff} ($0.6 \mu\text{m}$) absorption dominates over scattering for wavelengths above 8 μm , whereas absorption and scattering are of similar importance for larger r_{eff} ($\geq 1.8 \mu\text{m}$). The asymmetry parameter, Fig. 9 (c), increases with increasing r_{eff} , i.e. forward scattering becomes dominant.

Next we consider different particle shapes (spheres, pro- and oblate spheroids; $r \in [0.001, 30] \mu\text{m}$) and shape distributions (log-normal distributions of spheroids as described in Sec. 2.2.2; $r \in [0.001, 13] \mu\text{m}$). For aspect ratio distributions ε is limited to $[1, 5]$, split in 10 intervals. Pro- and oblate spheroids are used in equal parts. Considering different sizes (log-normal distribution with $r_{\text{eff}} \in \{0.6, 3, 6\} \mu\text{m}$, $s = 1.5$) we find that the shape has small influence on the optical properties with differences up to 10%, see Fig. 10 and Table 4.

To study the sensitivity with respect to the radius definition, we consider different possibilities (with $r \in [0.001, 13/12/9] \mu\text{m}$ for r_c , r_v and r_{vcr} , respectively) for different sizes (log-normal distribution with $r_{\text{eff}} \in \{0.6, 3, 6\} \mu\text{m}$, $s = 1.5$) and a non-spherical shape (pro- and oblate spheroids with log-normal aspect ratio distribution with $\varepsilon_0 = 1.5$ and $\sigma_{\text{ar}} = 0.45$), Fig. 11. The absolute differences are rather small although

Table 4

Maximal spreads (Δ) in the optical properties mass extinction coefficient (Ext.), single scattering albedo (SSA) and asymmetry parameter, and the corresponding wavelengths (λ) for the variation of different properties.

$r_{\text{eff}} / \mu\text{m}$	Ext. / $\frac{\text{m}^2}{\text{kg}}$		SSA		Asym. param.	
	Δ	$\lambda / \mu\text{m}$	Δ	$\lambda / \mu\text{m}$	Δ	$\lambda / \mu\text{m}$
–	301	9.6	0.64	7.9	0.79	8.1
			<i>Size</i>			
0.6	39	10.1	0.04	7.6	0.02	11.0
3.0	23	10.6	0.02	7.9	0.02	8.1
6.0	29	5.0	0.03	11.7	0.04	5.0
			<i>Shape</i>			
			<i>Radius definition</i>			
0.6	10	10.4	0.03	7.6	0.02	5.0
3.0	11	10.3	0.01	7.9	0.02	10.0
6.0	12	6.9	0.01	8.0	0.01	5.1
			<i>Composition (Refractive Index)</i>			
0.6	564	9.2	0.64	7.2	0.07	10.8
3.0	184	9.3	0.80	7.8	0.20	5.0
6.0	117	7.7	0.73	7.8	0.25	6.3

the relative differences can go up to about 17.5%. Generally, r_{ver} leads to larger differences from r_c than r_v . The differences tend to decrease with increasing r_{eff} .

Finally, we consider the influence of the volcanic ash composition (i.e. the refractive index and the corresponding bulk density) on the optical properties. Therefore, we consider spheres of different sizes (log-normal distribution with $r_{\text{eff}} \in \{0.6, 3, 6\} \mu\text{m}$, $s = 1.5$; $r \in [0.001, 20] \mu\text{m}$) and the refractive indices from Fig. 8 (but only $f_{\text{void}} = 0$ and $f_{\text{glass}} > 0$; 63 compositions in total). Note that this computation corresponds to assuming an internal mixture, since we use an effective refractive index for all particles in an ensemble, instead of different refractive indices of different glasses/minerals for the single particles. Although the main behavior of

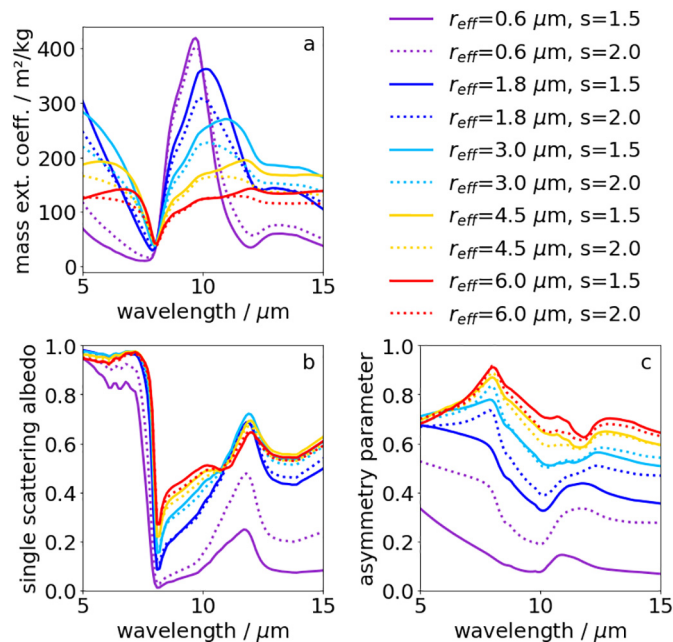


Fig. 9. Mass extinction coefficient (a), single scattering albedo (b) and asymmetry parameter (c) for ensembles of spherical particles with a log-normal size distribution with different r_{eff} and s with the refractive index of Eyjafjallajökull ash (Deguine et al. (2020)).

the optical properties is determined by r_{eff} , the refractive indices introduce a significant variability, see Fig. 12 and Table 4.

4. Discussions

Considering the refractive indices of volcanic glasses in Fig. 6, there are some general features observable. Up to 8 μm there is relatively little variation in the imaginary part, Fig. 6 (b), but significant variation for larger wavelengths. Similar results have been found by Reed et al. (2018). In the real part there is small variability approximately at 11 μm and 13 μm , Fig. 6 (a). Similar points appeared in the models of the refractive index of Prata et al. (2019). The peak of the imaginary part (of the broad feature, neglecting the small troughs due to single minerals) varies between roughly 10 μm for 75 wt.% and 11 μm for 45 wt.%, Fig. 6 (b). For comparison, in laboratory measurements peaks were found to be in the range 9 to 10 μm (Reed et al., 2018) or 10 to 10.5 μm (Deguine et al., 2020). The width of the peak varies also depending on the composition. In Prata et al. (2019) and Deguine et al. (2020), a shift of the peak towards higher wavelengths and an increase of width was shown to be connected to a lower silica content. Fig. 6 (b) shows a similar behavior for our volcanic glasses. Also the real part shows a similar dependence on the silica content as in Prata et al. (2019) and Deguine et al. (2020), e.g. a negative correlation of the refractive index and the silica content for wavelengths 5 to 8.5 μm and 11 to 15 μm , but a positive correlation for 9.5 to 11 μm , Fig. 6 (a). However, the amplitudes of the refractive indices are much smaller in Reed et al. (2018) and Prata et al. (2019). The comparison indicates that the qualitative behavior of volcanic glass and the bulk volcanic ash are similar. Note that we calculated the refractive indices of volcanic glasses using the data of Deguine et al. (2020) instead of the results of Reed et al. (2018), as R^2 using the latter is generally lower, Figs. 4 (c) and 5 (c). Deguine et al. (2020) also showed that their results are in better agreement with the glass refractive indices from Pollack et al. (1973) than the results by Reed et al. (2018). As pointed out by Deguine et al. (2020) different assumptions with respect to the shape (spheres and ellipsoids) might be the reason for the large differences in the refractive indices.

Fig. 8 allows us to estimate the importance of different compositional properties regarding the refractive indices. For instance the difference between the pure minerals (pink in Fig. 8) and the pure glass (solid black) is generally small, except for the typical quartz peaks between 9 and 10 μm . Also the influence of the minerals is more visible for volcanic ashes with $x_s = 45$ wt.%, Fig. 8 (a, b), which can also have more crystals, i.e. a lower f_{glass} . However, the porosity is significant, leading to a flattening of the real part n of the refractive index, Fig. 8 (a, c, e, g), and a lowering of the peak amplitude in the imaginary part k , Fig. 8 (b, d, f, h). Also the silica content x_s has a large impact: whereas the imaginary part k of the refractive index reaches up to about 1 for $x_s = 45$ wt.%, Fig. 8 (b), it increases up to about 1.5 for $x_s = 75$ wt.%, Fig. 8 (h).

We note that these results should be treated with some caution: we make various assumptions, each of them having a non-negligible impact. For instance the calculations are based on different refractive index measurements of minerals using different techniques and instruments, and some may be less accurate than others (e.g. anorthite does not become zero for small wavelengths, diopside exhibits some features that are very similar to quartz, Fig. 1). Also, all the minerals are investigated in form of KBr pellets or pure crystalline slabs, whereas the volcanic ash samples were measured in suspension in nitrogen gas (Reed et al., 2018; Deguine et al., 2020). Furthermore, we considered only a subset of all possible minerals in volcanic ash and assumed that all ashes of the same silica content have the same mineral phase distribution. Both assumptions might fail in specific cases. The volume weighted averaging is certainly valid for the density, but might have its limits for the refractive index. For instance, the refractive index of a particle consisting of a crystal covered by glass might be stronger influenced by the glass than by the mineral. Our assumptions for f_{void} and f_{glass}

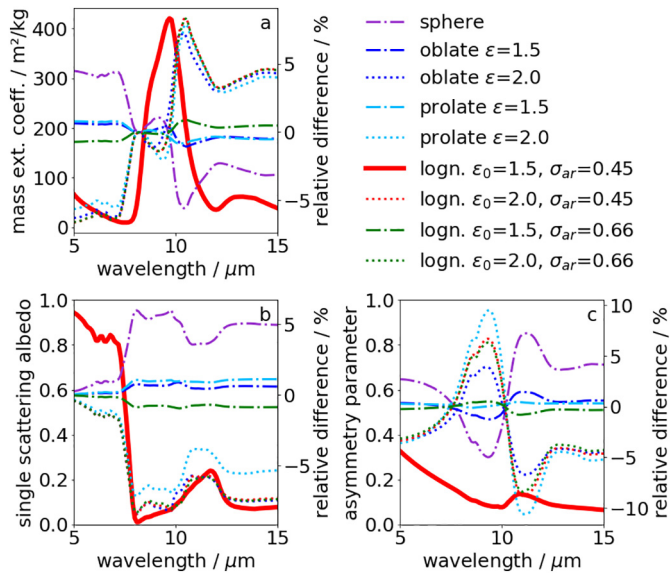


Fig. 10. Mass extinction coefficient (a), single scattering albedo (b) and asymmetry parameter (c) for particle ensembles with a log-normal size distribution with $r_{\text{eff}} = 0.6 \mu\text{m}$ and $s = 1.5$ with the refractive index of the Eyjafjallajökull ash by Deguine et al. (2020). Different shapes (spheres, spheroids) and aspect ratio distributions are considered. The latter are modified log-normal distributions consisting of ob- and prolate particles in equal parts with different ϵ_0 and σ_{ar} . One case (thick red line) is shown as reference (left axis), whereas for the others the relative differences are shown (right axis).

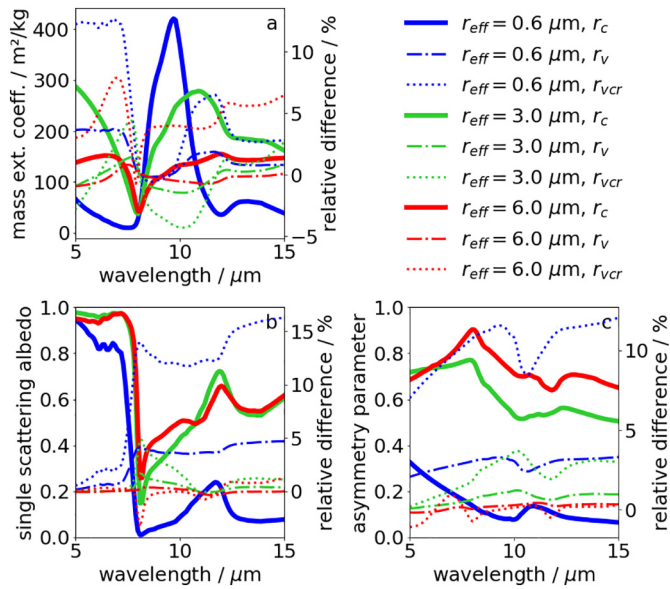


Fig. 11. Mass extinction coefficient (a), single scattering albedo (b) and asymmetry parameter (c) for ensembles of particles with a log-normal size distribution with different r_{eff} and $s = 1.5$, a log-normal aspect ratio distribution with $\epsilon_0 = 1.5$, $\sigma_{\text{ar}} = 0.45$ of spheroids, with the refractive index of the Eyjafjallajökull ash by Deguine et al. (2020). For the different r_{eff} different definitions of the radius are shown. One case (thick solid line) is shown as reference (left axis), whereas for the others the relative differences are shown (right axis).

are based on statistical analyses rather than on individual measurements. Especially a non-negligible porosity might significantly alter the derived refractive indices of volcanic glasses, Fig. 3 and Table 3. Also the assumption of bubbles filled with air instead of specific gases resulting in the approximations $m_{\text{void}} = 1$ and $\rho_{\text{void}} = 0$ should be mentioned here. For the calculation of the volcanic glasses we relied on the

measurements of Deguine et al. (2020). However, comparing these with Reed et al. (2018) shows that very similar measurement techniques might still result in different refractive indices. Also the refractive indices from both, Reed et al. (2018) and Deguine et al. (2020), do not show the large peaks of crystalline quartz, which leads to troughs in our volcanic glass refractive indices.

Comparing the results in Table 4 for the spreads in optical properties we see that with respect to the mass extinction coefficient the radius definition leads to the smallest variability, followed by the shape. Size and composition have a similar large impact in general, with the impact of the composition increasing with decreasing r_{eff} . Note that the maximum spread due to the composition is located at a wavelength of 9.2 to 9.3 μm for $r_{\text{eff}} = 0.6 \mu\text{m}$ and 3.0 μm , respectively, which is where the major quartz peak is located, Fig. 12 (a, b). Thus, a single crystal leads to this large impact. Considering the single scattering albedo the ranking of importance is the same. Here most maximum spreads are located at 7.3 to 8.0 μm . At this point the single scattering albedo drops from close to 1 to below 0.5. This drop can be slightly shifted, Fig. 9 (b), such that the maximum spread in this regime can be larger than the general variability. Finally, with respect to the asymmetry parameter the size leads to the largest spread, followed by the composition, followed by the shape and the radius definition. Based on these rankings we decide to incorporate the full variability due to size and composition to create our representative data set of optical properties for volcanic ash. Thus, the size distributions for all r_{eff} and s are considered, as well as all refractive indices. For shape and radius definition the impacts are relatively small such that a single setting is indeed sufficient. Thus, for the shape a log-normal distribution with $\epsilon_0 = 1.5$ and $\sigma_{\text{ar}} = 0.45$ and the radius definition r_c are used. The ranking also indicates that

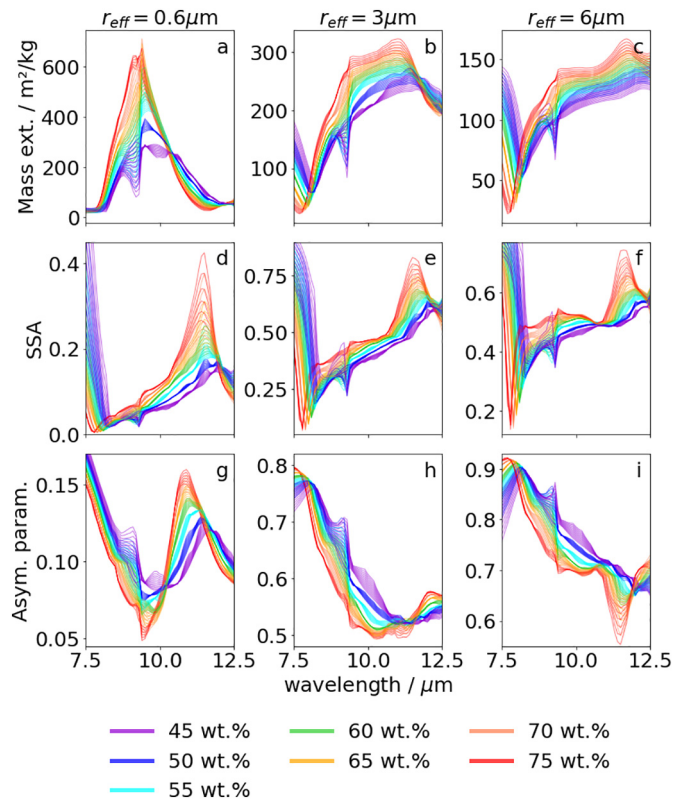


Fig. 12. Mass extinction coefficient (a, b, c), single scattering albedo (d, e, f) and asymmetry parameter (g, h, i) for ensembles of spherical particles with a log-normal size distribution with different r_{eff} and $s = 1.5$ for different refractive indices (see text). The different silica contents are marked by color.

mainly size and composition are needed for a fast calculation of the refractive index and the optical properties of a specific volcanic ash.

Regarding satellite remote sensing two further points should be stressed: First, the dominant peak of the mass extinction coefficient around 10 μm decreases with increasing r_{eff} , Fig. 9 (a), and finally vanishes, leading to a strong dependence of BTD_{11-12} on r_{eff} ; for $r_{\text{eff}} \geq 6 \mu\text{m}$ the signal in BTD_{11-12} might disappear or even become positive. This dependence has also been pointed out by Prata (1989); Wen and Rose (1994); Stevenson et al. (2015). Second, the dependency of the optical properties on the silica content is visible in Fig. 12. For instance for large particles ($r_{\text{eff}} = 6 \mu\text{m}$) the mass extinction coefficient correlates roughly with the silica content for 8.5 to 12 μm , Fig. 12 (c). However, for small particles ($r_{\text{eff}} = 0.6 \mu\text{m}$) the behavior changes in the regime 10 to 12 μm : here the quantities anti-correlate, Fig. 12 (a). Similar dependencies are visible for the single scattering albedo, Fig. 12 (d, e, f) and the asymmetry parameter, Fig. 12 (g, h, i). In particular the silica dependencies of the mass extinction coefficient, Fig. 12 (a, b, c), indicate that there might be a possibility to retrieve the silica content as a proxy for the composition by satellite.

As noted in the introduction, BTD_{11-12} can be considered for the detection of volcanic clouds via satellite. Using our representative set of optical properties (as outlined above and calculated for $r \in [0.001, 12] \mu\text{m}$) we determine BTD_{11-12} for an example (Sec. 2.3) of small particles ($r_{\text{eff}} = 0.6 \mu\text{m}$, $s = 1.5$). In this case neglecting scattering effects (Sec. 2.3) is valid as the single scattering albedo for these particles is below roughly 0.4, but there is large variability with respect to the composition, Fig. 12(a, d, g). BTD_{11-12} is then $-1.9 \pm 0.7 \text{ K}$ and ranges from -2.8 to -0.7 K , i.e. all BTD_{11-12} are negative for the specific size, Fig. 13. Note that the standard deviation is already larger than for instance the

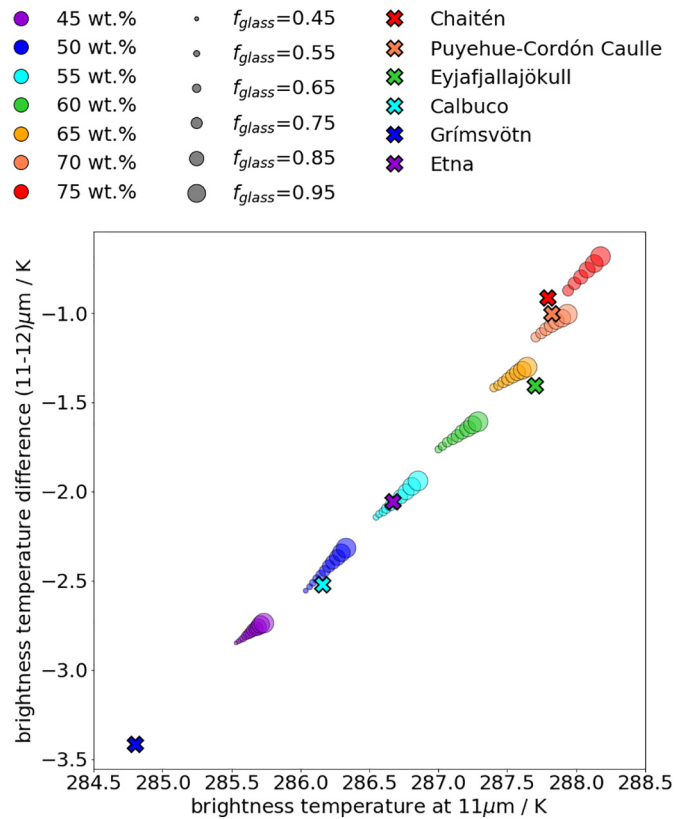


Fig. 13. Brightness temperature at 11 μm vs. brightness temperature difference at 11 μm and 12 μm for different compositions (as derived in Sec. 3.1), a log-normal size distribution ($r_{\text{eff}} = 0.6 \mu\text{m}$, $s = 1.5$), and a ob-/prolate spheroidal shape with a modified log-normal aspect ratio distribution ($\epsilon_0 = 1.5$, $\sigma_{\text{ar}} = 0.45$). Also marked are the results for the refractive indices from Deguine et al. (2020) for the same microphysical properties.

instrumental uncertainties of the 10.8 μm and 12.0 μm channels of the radiometer MSG-SEVIRI, which are of the order of 0.06 K and 0.10 to 0.16 K in-flight at 95 K (EUMETSAT, 2019; Schmetz et al., 2002b), stressing the importance to consider the correct composition in remote sensing retrieval applications. Fig. 13 shows that in this case different silica contents (indicated by the color) might be separable up to a certain degree. The size of the markers also indicates f_{glass} . Within this model an increase in f_{glass} leads to an increase in BTD_{11-12} . However, the differences from f_{glass} are much smaller than those due to x_s , and of a similar order as the instrumental noise. Crosses indicate the results for the refractive indices of Deguine et al. (2020). They are aligned along the results of our representative data set, but some show large deviations from our calculations of similar silica content, e.g. Grímsvötn. Its peak in the imaginary part is shifted to larger wavelengths, Fig. 5 and Deguine et al. (2020), which results in a more negative BTD_{11-12} . This shows that the variability of the refractive index of volcanic ash might be even larger than what is covered by our method.

5. Conclusions

Monitoring and initializing of nowcastings for volcanic ash clouds is regularly performed using satellite-borne passive infrared imagers. As these retrievals often rely on radiative transfer calculations, a good knowledge of the microphysical properties and the complex refractive index of volcanic ash is necessary. In this work we describe a method to calculate the complex refractive index of volcanic ash in the infrared (5 to 15 μm). This can be done for different volcanic ash compositions with respect to volcanic glasses, crystalline minerals and vesicles. The main parameters are the silica content, the glass fraction and the porosity. We compose a set of complex refractive indices in the infrared of the individual crystalline components as well as their densities. Combining these according to a typical silica dependent distribution from the literature we get effective refractive indices for the mineral part. These are used to determine the refractive indices of various volcanic glasses from the refractive indices of corresponding bulk samples from the literature. A wavelength dependent linear regression between the refractive indices of the volcanic glasses and the bulk silica content is performed. Subsequently, the refractive indices of the minerals and the glasses are combined for different compositions (varying silica content, glass fraction and porosity). Our results indicate that the impact of the glass fraction seems to be rather negligible compared to the impact of the silica content, which in turn may have less influence than the porosity. However, a short literature review indicates that the last might be negligible for particle sizes of the order of 1 μm , although this is not fully settled. The density of the volcanic ash was determined similar to the refractive index.

Furthermore, we review typical microphysical properties (size and shape) of volcanic ash. Calculating the resulting optical properties we show that the size and the composition lead to the largest variations with similar impact, whereas the considered shapes and radius definitions play a minor role. We show that the extinctions for 11 to 12 μm exhibit a size dependence such that the corresponding brightness temperature difference BTD_{11-12} might become non-negative, and thus the criterion $BTD_{11-12} < 0$ regularly applied for volcanic ash detection by satellite might not be applicable for roughly $r_{\text{eff}} \geq 6 \mu\text{m}$. A small single scattering albedo is observed for small particles, whereas scattering and absorption are more balanced for larger particles. Applying a simple model we estimate the range of BTD_{11-12} and find a strong dependence on the composition which is non-negligible for modern satellite instruments.

To improve our method further laboratory measurements of bulk volcanic ashes and volcanic glasses would be needed, preferably together with measurements of mineral compositions, glass fractions and porosities. The latter would enable us to further validate our calculations. But already now our work shows that the composition of volcanic ash and, therefore, a proper assumption of the refractive index is

necessary for trustworthy satellite retrievals in the infrared. The results can be used for the development of new retrieval algorithms or to quantify the uncertainties in radiative transfer calculation-based retrievals due to the usage of a single refractive index for the volcanic ash. Also noteworthy is the fact that a dependence on the silica content (and to a much smaller extent on the glass fraction) is observable in the refractive index, the mass extinction coefficient and $BTID_{11-12}$, indicating that composition might be retrievable to some degree by remote sensing methods.

Data availability

The created complex refractive indices of volcanic ash as well as the optical properties are available as supplementary data (Piontek et al., 2021).

Declaration of Competing Interest

None.

Acknowledgments

D. Piontek was supported by the European Unions's Horizon 2020 research and innovation program under grant agreement no. 723986 (EUNADICS-AV), J. Gasteiger under grant agreement no. 640458 (A-LIFE) and A. Hornby by grant agreement no. 753900 (Marie Skłodowska-Curie Action AVAST). C. Voigt acknowledges funding by the Helmholtz Association under contract HGF W2/W3-60. Work by D. Piontek, A. Hornby and C. Voigt was linked to and partially funded by the TeMaS research cluster (University Mainz). The volcanic ash refractive indices by Reed et al. (2018) and Deguine et al. (2020) have been made available through the ARIA database. We like to thank M. Vázquez-Navarro, M. Rapp, B. Mayer and D. Dingwell for the constructive discussions and valuable feedback, as well as R. Meerkötter, U. Schumann and two reviewers for their helpful comments to improve the manuscript.

References

- Arnold, J.A., Glotch, T.D., Plonka, A.M., 2014. Mid-infrared optical constants of clinopyroxene and orthoclase derived from oriented single-crystal reflectance spectra. *Am. Mineral.* 99, 1942–1955. <https://doi.org/10.2138/am-2014-4828>.
- Aronson, J.R., Strong, P.F., 1975. Optical constants of minerals and rocks. *Appl. Opt.* 14, 2914–2920. <https://doi.org/10.1364/AO.14.002914>.
- Ball, J.G.C., Reed, B.E., Grainger, R.G., Peters, D.M., Mather, T.A., Pyle, D.M., 2015. Measurements of the complex refractive index of volcanic ash at 450, 546.7, and 650 nm. *J. Geophys. Res. Atmos.* 120, 7747–7757. <https://doi.org/10.1002/2015JD023521>.
- Bessho, K., Date, K., Hayashi, M., Ikeda, A., Imai, T., Inoue, H., Kumagai, Y., Miyakawa, T., Murata, H., Ohno, T., Okuyama, A., Oyama, R., Sasaki, Y., Shimazu, Y., Shimoji, K., Sumida, Y., Suzuki, M., Taniguchi, H., Tsuchiyama, H., Uesawa, D., Yokota, H., Yoshida, R., 2016. An Introduction to Himawari-8/9 - Japan's New-Generation Geostationary Meteorological Satellites. *J. Meteorol. Soc. Jpn. Ser. II* 94, 151–183. <https://doi.org/10.2151/jmsj.2016-009>.
- Best, M.G., 2003. *Igneous and Metamorphic Petrology*. 2nd ed. Blackwell Science, Malden.
- Budd, L., Griggs, S., Howarth, D., Ison, S., 2011. A Fiasco of Volcanic Proportions? Eyjafjallajökull and the Closure of European Airspace. *Mobilities* 6, 31–40. <https://doi.org/10.1080/17450101.2011.532650>.
- Casadevall, T.J., 1994. The 1989–1990 eruption of Redoubt Volcano, Alaska: impacts on aircraft operations. *J. Volcanol. Geotherm. Res.* 62, 301–316. [https://doi.org/10.1016/0377-0273\(94\)90038-8](https://doi.org/10.1016/0377-0273(94)90038-8).
- Casas, A.S., Wadsworth, F.B., Ayris, P.M., Delmelle, P., Vasseur, J., Cimarelli, C., Dingwell, D.B., 2019. SO₂ scrubbing during percolation through rhyolitic volcanic domes. *Geochim. Cosmochim. Acta* 257, 150–162. <https://doi.org/10.1016/j.gca.2019.04.013>.
- Cioni, R., Pistolesi, M., Bertagnini, A., Bonadonna, C., Hoskuldsson, A., Scateni, B., 2014. Insights into the dynamics and evolution of the 2010 Eyjafjallajökull summit eruption (Iceland) provided by volcanic ash textures. *Earth Planet. Sci. Lett.* 394, 111–123. <https://doi.org/10.1016/j.epsl.2014.02.051>.
- Clarisse, L., Prata, F., Lacour, J.L., Hurtmans, D., Clerbaux, C., Coheur, P.F., 2010. A correlation method for volcanic ash detection using hyperspectral infrared measurements. *Geophys. Res. Lett.* 37. <https://doi.org/10.1029/2010GL044828>.
- Clark, S.P., 1966. *Handbook of Physical Constants*. Geological Society of America, New York.
- Colucci, S., Palladino, D.M., Mulukutla, G.K., Proussevitch, A.A., 2013. 3-D reconstruction of ash vesicularity: Insights into the origin of ash-rich explosive eruptions. *J. Volcanol. Geotherm. Res.* 255, 98–107. <https://doi.org/10.1016/j.jvolgeores.2013.02.002>.
- Cooper, B.L., Salisbury, J.W., Killen, R.M., Potter, A.E., 2002. Midinfrared spectral features of rocks and their powders. *J. Geophys. Res. Planets* 107. <https://doi.org/10.1029/2000JE001462> 1–1–1–17.
- Dacre, H.F., Harvey, N.J., Webley, P.W., Morton, D., 2016. How accurate are volcanic ash simulations of the 2010 Eyjafjallajökull eruption? *J. Geophys. Res. Atmos.* 121, 3534–3547. <https://doi.org/10.1002/2015JD024265>.
- Deguine, A., Petitprez, D., Clarisse, L., Gudmundsson, S., Outes, V., Villarosa, G., Herbin, H., 2020. Complex refractive index of volcanic ash aerosol in the infrared, visible, and ultraviolet. *Appl. Opt.* 59, 884–895. <https://doi.org/10.1364/AO.59.000884>.
- Delmelle, P., Villiéras, F., Pelletier, M., 2005. Surface area, porosity and water adsorption properties of fine volcanic ash particles. *Bull. Volcanol.* 67, 160–169. <https://doi.org/10.1007/s00445-004-0370-x>.
- Ebert, M., Weinbruch, S., Rausch, A., Gorzawski, G., Helas, G., Hoffmann, P., Wex, H., 2002. Complex refractive index of aerosols during LACE 98 as derived from the analysis of individual particles. *J. Geophys. Res. Atmos.* 107. <https://doi.org/10.1029/2000JD000195> LAC 3–1–LAC 3–15.
- EUMETSAT, 2019. *Typical Radiometric Noise, Calibration Bias and Stability for Meteosat-8, -9, -10 and -11 SEVIRI*.
- Farlow, N.H., Orberbeck, V.R., Snetsinger, K.G., Ferry, G.V., Polkowski, G., Hayes, D.M., 1981. Size Distributions and Mineralogy of Ash Particles in the Stratosphere from Eruptions of Mount St. Helens. *Science* 211, 832–834. <https://doi.org/10.1126/science.211.4484.832>.
- Francis, P.N., Cooke, M.C., Saunders, R.W., 2012. Retrieval of physical properties of volcanic ash using Meteosat: A case study from the 2010 Eyjafjallajökull eruption. *J. Geophys. Res. Atmos.* 117. <https://doi.org/10.1029/2011JD016788>.
- Freundt, A., Schmincke, H.U., 1992. Mixing of rhyolite, trachyte and basalt magma erupted from a vertically and laterally zoned reservoir, composite flow P1, Gran Canaria. *Contrib. Mineral. Petrol.* 112, 1–19. <https://doi.org/10.1007/BF00310952>.
- Gangale, G., Prata, A., Clarisse, L., 2010. The infrared spectral signature of volcanic ash determined from high-spectral resolution satellite measurements. *Remote Sens. Environ.* 114, 414–425. <https://doi.org/10.1016/j.rse.2009.09.007>.
- Gasteiger, J., Wiegner, M., 2018. MOPSMAP v1.0: a versatile tool for the modeling of aerosol optical properties. *Geosci. Model Dev.* 11, 2739–2762. <https://doi.org/10.5194/gmd-11-2739-2018>.
- Genareau, K., Proussevitch, A.A., Durant, A.J., Mulukutla, G., Sahagian, D.L., 2012. Sizing up the bubbles that produce very fine ash during explosive volcanic eruptions. *Geophys. Res. Lett.* 39. <https://doi.org/10.1029/2012GL052471>.
- Genareau, K., Mulukutla, G.K., Proussevitch, A.A., Durant, A.J., Rose, W.I., Sahagian, D.L., 2013. The size range of bubbles that produce ash during explosive volcanic eruptions. *J. Appl. Volcanol.* 2, 4. <https://doi.org/10.1186/2191-5040-2-4>.
- Glotch, T.D., Rossman, G.R., 2009. Mid-infrared reflectance spectra and optical constants of six iron oxide/oxyhydroxide phases. *Icarus* 204, 663–671. <https://doi.org/10.1016/j.icarus.2009.07.024>.
- Grainger, R.G., Peters, D.M., Thomas, G.E., Smith, A.J.A., Siddans, R., Carboni, E., Dudhia, A., 2013. Measuring volcanic plume and ash properties from space. *Geol. Soc. Spec. Publ.* 380, 293–320. <https://doi.org/10.1144/SP380.7>.
- Gudmundsson, M.T., Thordarson, T., Höskuldsson, Á., Larsen, G., Björnsson, H., Prata, F.J., Oddsson, B., Magnússon, E., Högnadóttir, T., Petersen, G.N., Hayward, C.L., Stevenson, J.A., Jónsdóttir, I., 2012. Ash generation and distribution from the April–May 2010 eruption of Eyjafjallajökull, Iceland. *Sci. Rep.* 2, 572. <https://doi.org/10.1038/srep00572>.
- Guéhenneux, Y., Gouhier, M., Labazuy, P., 2015. Improved space borne detection of volcanic ash for real-time monitoring using 3-Band method. *J. Volcanol. Geotherm. Res.* 293, 25–45. <https://doi.org/10.1016/j.jvolgeores.2015.01.005>.
- Guffanti, M., Casadevall, T.J., Budding, K., 2010. Encounters of aircraft with volcanic ash clouds: A compilation of known incidents, 1953–2009. U.S. Geological Survey Data Series 545, ver. 1.0, 12 p., plus 4 appendixes including the compilation database. U.S. Geological Survey <http://pubs.usgs.gov/ds/545>.
- Haldar, S.K., Tišljár, J., 2014. *Introduction to Mineralogy and Petrology*. 1st ed. Elsevier, Amsterdam.
- Hansell Jr., R.A., Reid, J.S., Tsay, S.C., Roush, T.L., Kalashnikova, O.V., 2011. A sensitivity study on the effects of particle chemistry, asphericity and size on the mass extinction efficiency of mineral dust in the earth's atmosphere: from the near to thermal IR. *Atmos. Chem. Phys.* 11, 1527–1547. <https://doi.org/10.5194/acp-11-1527-2011>.
- Heiken, G., 1974. An Atlas of Volcanic Ash. *Smithson. Contrib. Earth Sci.* 12. <https://doi.org/10.5479/si.00810274.12.1>.
- Herbin, H., Pujol, O., Hubert, P., Petitprez, D., 2017. New approach for the determination of aerosol refractive indices – Part I: Theoretical bases and numerical methodology. *J. Quant. Spectrosc. Radiat. Transf.* 200, 311–319. <https://doi.org/10.1016/j.jqsrt.2017.03.005>.
- Hornby, A.J., Lavallée, Y., Kendrick, J.E., Rollinson, G., Butcher, A.R., Clesham, S., Kueppers, U., Cimarelli, C., Chigna, G., 2019. Phase partitioning during fragmentation revealed by QEMSCAN Particle Mineralogical Analysis of volcanic ash. *Sci. Rep.* 9, 126. <https://doi.org/10.1038/s41598-018-36857-4>.
- Inoue, T., 1985. On the Temperature and Effective Emissivity Determination of Semi-Transparent Cirrus Clouds by Bi-Spectral Measurements in the 10 μm Window Region. *J. Meteorol. Soc. Jpn.* 63, 88–99. <https://doi.org/10.2151/jmsj1965.63.1.88>.
- Ishimoto, H., Masuda, K., Fukui, K., Shimbori, T., Inazawa, T., Tsuchiyama, H., Ishii, K., Sakurai, T., 2016. Estimation of the refractive index of volcanic ash from satellite infrared sounder data. *Remote Sens. Environ.* 174, 165–180. <https://doi.org/10.1016/j.rse.2015.12.009>.
- Jerram, D., Petford, N., 2011. *The Field Description of Igneous Rocks*. 2nd ed. Wiley and Blackwell, Chichester.

- Kandler, K., Benker, N., Bundke, U., Cuevas, E., Ebert, M., Knippertz, P., Rodríguez, S., Schütz, L., Weinbruch, S., 2007. Chemical composition and complex refractive index of Saharan Mineral Dust at Izaña, Tenerife (Spain) derived by electron microscopy. *Atmos. Environ.* 41, 8058–8074. <https://doi.org/10.1016/j.atmosenv.2007.06.047>.
- Kitamura, R., Pilon, L., Jonasz, M., 2007. Optical constants of silica glass from extreme ultraviolet to far infrared at near room temperature. *Appl. Opt.* 46, 8118–8133. <https://doi.org/10.1364/AO.46.008118>.
- Klug, C., Cashman, K.V., 1994. Vesiculation of May 18, 1980, Mount St. Helens magma. *Geology* 22, 468–472. [https://doi.org/10.1130/0091-7613\(1994\)022<0468:VOMMSH>2.3.CO;2](https://doi.org/10.1130/0091-7613(1994)022<0468:VOMMSH>2.3.CO;2).
- Klüser, L., Erbertseder, T., Meyer-Arneke, J., 2013. Observation of volcanic ash from Puyehue–Cordón Caulle with IASI. *Atmos. Meas. Tech.* 6, 35–46. <https://doi.org/10.5194/amt-6-35-2013>.
- Koike, C., Hasegawa, H., Asada, N., Komatuzaki, T., 1989. Optical constants of fine particles for the infrared region. *Mon. Not. R. Astron. Soc.* 239, 127–137. <https://doi.org/10.1093/mnras/239.1.127>.
- Kylling, A., Kahnert, M., Lindqvist, H., Nousiainen, T., 2014. Volcanic ash infrared signature: porous non-spherical ash particle shapes compared to homogeneous spherical ash particles. *Atmos. Meas. Tech.* 7, 919–929. <https://doi.org/10.5194/amt-7-919-2014>.
- Langmann, B., 2013. Volcanic Ash versus Mineral Dust: Atmospheric Processing and Environmental and Climate Impacts. *ISRN Atmos. Sci.* 2013. <https://doi.org/10.1155/2013/245076>.
- Lee, K.M., Park, J.H., 2014. Optical constants for Asian dust in midinfrared region. *J. Geophys. Res. Atmos.* 119, 927–942. <https://doi.org/10.1002/2013JD020207>.
- Lee, K.H., Wong, M.S., Chung, S.R., Sohn, E., 2014. Improved volcanic ash detection based on a hybrid reverse absorption technique. *Atmos. Res.* 143, 31–42. <https://doi.org/10.1016/j.atmosres.2014.01.019>.
- Lesins, G., Chylek, P., Lohmann, U., 2002. A study of internal and external mixing scenarios and its effect on aerosol optical properties and direct radiative forcing. *J. Geophys. Res. Atmos.* 107. <https://doi.org/10.1029/2001JD000973> AAC 5–1–AAC 5–12.
- Limpert, E., Stahel, W.A., Abbt, M., 2001. Log-normal Distributions across the Sciences: Keys and Clues. *BioScience* 51, 341–352. [https://doi.org/10.1641/0006-3568\(2001\)051\[0341.LNDATS\]2.0.CO;2](https://doi.org/10.1641/0006-3568(2001)051[0341.LNDATS]2.0.CO;2).
- Lucarini, V., Saarinen, J.J., Peiponen, K., Vartiainen, E., 2005. *Kramers-Kronig Relations in Optical Materials Research*. Springer Science+Business Media, Berlin <https://doi.org/10.1007/b138913>.
- Mackie, S., Cashman, K., Ricketts, H., Rust, A., Watson, M. (Eds.), 2016. *Volcanica Ash: Hazard Observation*, 1st ed. Elsevier, Amsterdam.
- Mills, O.P., Rose, W.I., 2010. Shape and surface area measurements using scanning electron microscope stereo-pair images of volcanic ash particles. *Geosphere* 6, 805–811. <https://doi.org/10.1130/GES00558.1>.
- Miwa, T., Shimano, T., Nishimura, T., 2015. Characterization of the luminance and shape of ash particles at Sakurajima volcano, Japan, using CCD camera images. *Bull. Volcanol.* 77, 5. <https://doi.org/10.1007/s00445-014-0886-7>.
- Mukai, T., Koike, C., 1990. Optical Constants of Olivine Particles between Wavelengths of 7 and 200 μm . *Icarus* 87, 180–187. [https://doi.org/10.1016/0019-1035\(90\)90027-7](https://doi.org/10.1016/0019-1035(90)90027-7).
- Mutschke, H., Begemann, B., Dorschner, J., Guertler, J., Gustafson, B., Henning, T., Stognienko, R., 1998. Steps toward interstellar silicate mineralogy. III. The role of aluminium in circumstellar amorphous silicates. *Astron. Astrophys.* 333, 188–198.
- Nakagawa, M., Ohba, T., 2002. *Minerals in Volcanic Ash 1: Primary Minerals and Volcanic Glass*. *Glob. Environ. Res.* 6, 41–51.
- Newman, S.M., Clarisse, L., Hurtmans, D., Marengo, F., Johnson, B., Turnbull, K., Havemann, S., Baran, A.J., O'Sullivan, D., Haywood, J., 2012. A case study of observations of volcanic ash from the Eyjafjallajökull eruption: 2. Airborne and satellite radiative measurements. *J. Geophys. Res. Atmos.* 117. <https://doi.org/10.1029/2011JD016780>.
- Pavlonis, M.J., Feltz, W.F., Heidinger, A.K., Gallina, G.M., 2006. A Daytime Complement to the Reverse Absorption Technique for Improved Automated Detection of Volcanic Ash. *J. Atmos. Ocean. Technol.* 23, 1422–1444. <https://doi.org/10.1175/JTECH1926.1>.
- Pavlonis, M.J., Heidinger, A.K., Sieglaff, J., 2013. Automated retrievals of volcanic ash and dust cloud properties from upwelling infrared measurements. *J. Geophys. Res. Atmos.* 118, 1436–1458. <https://doi.org/10.1002/jgrd.50173>.
- Pavlonis, M.J., Sieglaff, J., Cintineo, J., 2015. Spectrally Enhanced Cloud Objects—A generalized framework for automated detection of volcanic ash and dust clouds using passive satellite measurements: 1. Multispectral analysis. *J. Geophys. Res. Atmos.* 120, 7813–7841. <https://doi.org/10.1002/2014JD022968>.
- Peterson, J.T., Weinman, J.A., 1969. Optical Properties of Quartz Dust Particles at Infrared Wavelengths. *J. Geophys. Res.* 74, 6947–6952. <https://doi.org/10.1029/JC074i028p06947>.
- Piontek, D., Hornby, A.J., Voigt, C., Bugliari, N., Gasteiger, J., 2021. Determination of complex refractive indices and optical properties of volcanic ashes in the thermal infrared based on generic petrological compositions: supplementary material. Zenodo <https://doi.org/10.5281/zenodo.4447877>.
- Piscini, A., Picchiani, M., Chini, M., Corradini, S., Merucci, L., Del Frate, F., Stramondo, S., 2014. A neural network approach for the simultaneous retrieval of volcanic ash parameters and SO₂ using MODIS data. *Atmos. Meas. Tech.* 7, 4023–4047. <https://doi.org/10.5194/amt-7-4023-2014>.
- Polacci, M., Andronico, D., de Micheli Vitturi, M., Taddeucci, J., Cristaldi, A., 2019. Mechanisms of Ash Generation at Basaltic Volcanoes: The Case of Mount Etna, Italy. *Front. Earth Sci.* 7, 193. <https://doi.org/10.3389/feart.2019.00193>.
- Pollack, J.B., Toon, O.B., Khare, B.N., 1973. Optical Properties of Some Terrestrial Rocks and Glasses. *Icarus* 19, 372–389. [https://doi.org/10.1016/0019-1035\(73\)90115-2](https://doi.org/10.1016/0019-1035(73)90115-2).
- Prata, A.J., 1989. Infrared radiative transfer calculations for volcanic ash clouds. *Geophys. Res. Lett.* 16, 1293–1296. <https://doi.org/10.1029/GL016i011p01293>.
- Prata, A.J., Grant, I.F., 2001. Retrieval of microphysical and morphological properties of volcanic ash plumes from satellite data: Application to Mt Ruapehu, New Zealand. *Q. J. R. Meteorol. Soc.* 127, 2153–2179. <https://doi.org/10.1002/qj.49712757615>.
- Prata, A.J., Prata, A.T., 2012. Eyjafjallajökull volcanic ash concentrations determined using Spin Enhanced Visible and Infrared Imager measurements. *J. Geophys. Res. Atmos.* 117. <https://doi.org/10.1029/2011JD016800>.
- Prata, G.S., Ventress, L.J., Carboni, E., Mather, T.A., Grainger, R.G., Pyle, D.M., 2019. A New Parameterization of Volcanic Ash Complex Refractive Index Based on NBO/T and SiO₂ Content. *J. Geophys. Res. Atmos.* 124, 1779–1797. <https://doi.org/10.1029/2018JD028679>.
- Pugnaghi, S., Guerrieri, L., Corradini, S., Merucci, L., Arvani, B., 2013. A new simplified approach for simultaneous retrieval of SO₂ and ash content of tropospheric volcanic clouds: an application to the Mt Etna volcano. *Atmos. Meas. Tech.* 6, 1315–1327. <https://doi.org/10.5194/amt-6-1315-2013>.
- Querry, M.R., 1983. *Optical Properties of Natural Minerals and Other Materials in the 350–50,000 cm⁻¹ Spectral Region*. Technical Report. University of Missouri Kansas City, Department of Physics.
- Ralph, J., 2020a. Mindat.org. <https://www.mindat.org/min-3231.html> (Online; accessed 17-July-2020).
- Ralph, J., 2020b. Mindat.org. <https://www.mindat.org/min-96.html> (Online; accessed 17-July-2020).
- Ralph, J., 2020c. Mindat.org. <https://www.mindat.org/min-246.html> (Online; accessed 17-July-2020).
- Ralph, J., 2020d. Mindat.org. <https://www.mindat.org/min-2815.html> (Online; accessed 17-July-2020).
- Ralph, J., 2020e. Mindat.org. <https://www.mindat.org/min-2538.html> (Online; accessed 17-July-2020).
- Reed, B.E., Peters, D.M., McPheat, R., Grainger, R.G., 2018. The Complex Refractive Index of Volcanic Ash Aerosol Retrieved From Spectral Mass Extinction. *J. Geophys. Res. Atmos.* 123, 1339–1350. <https://doi.org/10.1002/2017JD027362>.
- Reubi, O., Blundy, J., 2009. A dearth of intermediate melts at subduction zone volcanoes and the petrogenesis of arc andesites. *Nature* 461, 1269–1273. <https://doi.org/10.1038/nature08510>.
- Riley, C.M., Rose, W.I., Bluth, G.J.S., 2003. Quantitative shape measurements of distal volcanic ash. *J. Geophys. Res. Solid Earth* 108. <https://doi.org/10.1029/2001JB000818>.
- Rogers, N., 2015. *The Composition and Origin of Magma*. In: Sigurdsson, H., Houghton, B., McNutt, S.R., Rymer, H., Stix, J. (Eds.), *The Encyclopedia of Volcanoes*, 2nd ed. Academic Press, London, pp. 93–112.
- Rose, William I.J., 1977. Scavenging of volcanic aerosol by ash: Atmospheric and volcanological implications. *Geology* 5, 621–624. [https://doi.org/10.1130/0091-7613\(1977\)5\[621:SOVABA\]2.0.CO;2](https://doi.org/10.1130/0091-7613(1977)5[621:SOVABA]2.0.CO;2).
- Rose, W.I., Chuan, R.L., Cadle, R.D., Woods, D.C., 1980. Small Particles in Volcanic Eruption Clouds. *Am. J. Sci.* 280, 671–696. <https://doi.org/10.2475/ajs.280.8.671>.
- Rose, W.I., Riley, C.M., Darteville, S., 2003. Sizes and Shapes of 10-Ma Distal Fall Pyroclasts in the Ogallala Group, Nebraska. *J. Geol.* 111, 115–124. <https://doi.org/10.1086/344668>.
- Roush, T., Pollack, J., Orenberg, J., 1991. Derivation of Midinfrared (5–25 μm) Optical Constants of Some Silicates and Palagonite. *Icarus* 94, 191–208. [https://doi.org/10.1016/0019-1035\(91\)90150-R](https://doi.org/10.1016/0019-1035(91)90150-R).
- Schmetz, J., Pili, P., Tjemkes, S., Just, D., Kerkmann, J., Rota, S., Ratier, A., 2002a. An introduction to Meteosat Second Generation (MSG). *Bull. Am. Meteorol. Soc.* 83, 977–992. [https://doi.org/10.1175/1520-0477\(2002\)083<0977:AITMSG>2.3.CO;2](https://doi.org/10.1175/1520-0477(2002)083<0977:AITMSG>2.3.CO;2).
- Schmetz, J., Pili, P., Tjemkes, S., Just, D., Kerkmann, J., Rota, S., Ratier, A., 2002b. Radiometric performance of SEVIRI. *Bull. Am. Meteorol. Soc.* 83, ES50–ES51. <https://doi.org/10.1175/BAMS-83-7-Schmetz-1>.
- Schmit, T.J., Gunshor, M.M., Menzel, W.P., Gurka, J.J., Li, J., Bachmeier, A.S., 2005. Introducing the Next-Generation Advanced Baseline Imager on GOES-R. *Bull. Am. Meteorol. Soc.* 86, 1079–1096. <https://doi.org/10.1175/BAMS-86-8-1079>.
- Schumann, U., Weinzierl, B., Reitebuch, O., Schlager, H., Minikin, A., Forster, C., Baumann, R., Sailer, T., Graf, K., Mannstein, H., Voigt, C., Rahm, S., Simmet, R., Scheibe, M., Lichtenstern, M., Stock, P., Rüba, H., Schäuble, D., Tafferner, A., Rautenhaus, M., Gerz, T., Ziereis, H., Krautstrunk, M., Mallaun, C., Gayet, J.F., Lieke, K., Kandler, K., Ebert, M., Weinbruch, S., Stohl, A., Gasteiger, J., Groß, S., Freudenthaler, V., Wiegner, M., Ansmann, A., Tesche, M., Olafsson, H., Sturm, K., 2011. Airborne observations of the Eyjafjalla volcano ash cloud over Europe during air space closure in April and May 2010. *Atmos. Chem. Phys.* 11, 2245–2279. <https://doi.org/10.5194/acp-11-2245-2011>.
- Sen, G., 2014. *Petrology: Principles and Practice*, 1st ed. Springer-Verlag, Berlin Heidelberg.
- Shcherbakov, V., Jourdan, O., Voigt, C., Gayet, J.F., Chauvigne, A., Schwarzenboeck, A., Minikin, A., Klingebiel, M., Weigel, R., Borrmann, S., Jurkat, T., Kaufmann, S., Schlager, R., Gourbeyre, C., Febvre, G., Lapyonok, T., Frey, W., Moller, S., Weinzierl, B., 2016. Porous aerosol in degassing plumes of Mt. Etna and Mt. Stromboli. *Atmos. Chem. Phys.* 16, 11883–11897. <https://doi.org/10.5194/acp-16-11883-2016>.
- Shiple, S., Sarna-Wojcicki, A.M., 1982. Distribution, thickness, and mass of late pleistocene and holocene tephra from major volcanoes in the northwestern United States: a preliminary assessment of hazards from volcanic ejecta to nuclear reactors in the Pacific northwest. *U.S. Geol. Surv. Misc. Field Stud. Map MF-1435*.
- Sokolik, I.N., Toon, O.B., 1999. Incorporation of mineralogical composition into models of the radiative properties of mineral aerosol from UV to IR wavelengths. *J. Geophys. Res. Atmos.* 104, 9423–9444. <https://doi.org/10.1029/1998JD200048>.
- Sparks, R., 1978. The dynamics of bubble formation and growth in magmas: A review and analysis. *J. Volcanol. Geotherm. Res.* 3, 1–37. [https://doi.org/10.1016/0377-0273\(78\)90002-1](https://doi.org/10.1016/0377-0273(78)90002-1).
- Spitzer, W.G., Kleinman, D.A., 1961. Infrared Lattice Bands of Quartz. *Phys. Rev.* 121, 1324–1335. <https://doi.org/10.1103/PhysRev.121.1324>.

- Stevenson, J.A., Millington, S.C., Beckett, F.M., Swindles, G.T., Thordarson, T., 2015. Big grains go far: understanding the discrepancy between tephrochronology and satellite infrared measurements of volcanic ash. *Atmos. Meas. Tech.* 8, 2069–2091. <https://doi.org/10.5194/amt-8-2069-2015>.
- Stohl, A., Prata, A.J., Eckhardt, S., Clarisse, L., Durant, A., Henne, S., Kristiansen, N.I., Minikin, A., Schumann, U., Seibert, P., Stebel, K., Thomas, H.E., Thorsteinsson, T., Tørseth, K., Weinzierl, B., 2011. Determination of time- and height-resolved volcanic ash emissions and their use for quantitative ash dispersion modeling: the 2010 Eyjafjallajökull eruption. *Atmos. Chem. Phys.* 11, 4333–4351. <https://doi.org/10.5194/acp-11-4333-2011>.
- Vedder, W., 1964. Correlations between infrared spectrum and chemical composition of mica. *Am. Mineral.* 49, 736–768.
- Vogel, A., Diplas, S., Durant, A.J., Azar, A.S., Sunding, M.F., Rose, W.I., Sytchkova, A., Bonadonna, C., Krüger, K., Stohl, A., 2017. Reference data set of volcanic ash physico-chemical and optical properties. *J. Geophys. Res. Atmos.* 122, 9485–9514. <https://doi.org/10.1002/2016JD026328>.
- Volz, F.E., 1973. Infrared Optical Constants of Ammonium Sulfate, Sahara Dust, Volcanic Pumice, and Flyash. *Appl. Opt.* 12, 564–568. <https://doi.org/10.1364/AO.12.000564>.
- Wakaki, M., Kudo, K., Shibuya, T., 2007. *Physical Properties and Data of Optical Materials*. 1st ed. CRC Press, Boca Raton.
- Watkin, S.C., 2003. The application of AVHRR data for the detection of volcanic ash in a Volcanic Ash Advisory Centre. *Meteorol. Appl.* 10, 301–311. <https://doi.org/10.1017/S1350482703001063>.
- Watson, I., Realmuto, V., Rose, W., Prata, A., Bluth, G., Gu, Y., Bader, C., Yu, T., 2004. Thermal infrared remote sensing of volcanic emissions using the moderate resolution imaging spectroradiometer. *J. Volcanol. Geotherm. Res.* 135, 75–89. <https://doi.org/10.1016/j.jvolgeores.2003.12.017>.
- Wen, S., Rose, W.I., 1994. Retrieval of sizes and total masses of particles in volcanic clouds using AVHRR bands 4 and 5. *J. Geophys. Res. Atmos.* 99, 5421–5431. <https://doi.org/10.1029/93JD03340>.
- Western, L.M., Watson, M.I., Francis, P.N., 2015. Uncertainty in two-channel infrared remote sensing retrievals of a well-characterised volcanic ash cloud. *Bull. Volcanol.* 77, 67. <https://doi.org/10.1007/s00445-015-0950-y>.
- Wilson, T.M., Stewart, C., Sword-Daniels, V., Leonard, G.S., Johnston, D.M., Cole, J.W., Wardman, J., Wilson, G., Barnard, S.T., 2012. Volcanic ash impacts on critical infrastructure. *Phys. Chem. Earth* 45–46, 5–23. <https://doi.org/10.1016/j.pce.2011.06.006>.
- Wohletz, K.H., Sheridan, M.F., Brown, W.K., 1989. Particle Size Distributions and the Sequential Fragmentation/Transport Theory Applied to Volcanic Ash. *J. Geophys. Res. Solid Earth* 94, 15703–15721. <https://doi.org/10.1029/JB094iB11p15703>.
- Ye, C., Rucks, M.J., Arnold, J.A., Glotch, T.D., 2019. Mid-Infrared Optical Constants of Labradorite, a Triclinic Plagioclase Mineral. *Earth Space Sci.* 6, 2410–2422. <https://doi.org/10.1029/2019EA000915>.
- Yu, T., Rose, W.I., Prata, A.J., 2002. Atmospheric correction for satellite-based volcanic ash mapping and retrievals using “split window” IR data from GOES and AVHRR. *J. Geophys. Res. Atmos.* 107. <https://doi.org/10.1029/2001JD000706> AAC 10–1–AAC 10–19.
- Zhou, D.K., Larar, A.M., Liu, X., 2013. MetOp-A/IASI Observed Continental Thermal IR Emissivity Variations. *IEEE J. Sel. Top. Appl. Earth Obs. Remote Sens.* 6, 1156–1162.